Remote Sensing of Environment 273 (2022) 112985

Contents lists available at ScienceDirect

Remote Sensing of Environment

journal homepage: www.elsevier.com/locate/rse

Development of the GLASS 250-m leaf area index product (version 6) from MODIS data using the bidirectional LSTM deep learning model

Han Ma [a], Shunlin Liang [b,*]

[a] School of Remote Sensing and Information Engineering, Wuhan University, Hubei 430010, China
[b] Department of Geographical Sciences, University of Maryland, College Park, MD 20742, USA

ARTICLE INFO

Editor: Youngryel Ryu

Keywords:
Leaf area index
GLASS
MODIS
PROBA-V
Deep learning
LSTM

ABSTRACT

Leaf area index (LAI) is a terrestrial essential climate variable that is required in a variety of ecosystem and climate models. The Global LAnd Surface Satellite (GLASS) LAI product has been widely used, but its current version (V5) from Moderate Resolution Imaging Spectroradiometer (MODIS) data has several limitations, such as frequent temporal fluctuation, large data gaps, high dependence on the quality of surface reflectance, and low computational efficiency. To address these issues, this paper presents a deep learning model to generate a new version of the LAI product (V6) at 250-m resolution from MODIS data from 2000 onward. Unlike most existing algorithms that estimate one LAI value at one time for each pixel, this model estimates LAI for 2 years simultaneously. Three widely used LAI products (MODIS C6, GLASS V5, and PROBA-V V1) are used to generate global representative time-series LAI training samples using K-means clustering analysis and least difference criteria. We explore four machine learning models, the general regression neural network (GRNN), long short-term memory (LSTM), gated recurrent unit (GRU), and Bidirectional LSTM (Bi-LSTM), and identify Bi-LSTM as the best model for product generation. This new product is directly validated using 79 high-resolution LAI reference maps from three in situ observation networks. The results show that GLASS V6 LAI achieves higher accuracy, with a root mean square (RMSE) of 0.92 at 250 m and 0.86 at 500 m, while the RMSE is 0.98 for PROBA-V at 300 m, 1.08 for GLASS V5, and 0.95 for MODIS C6 both at 500 m. Spatial and temporal consistency analyses also demonstrate that the GLASS V6 LAI product is more spatiotemporally continuous and has higher quality in terms of presenting more realistic temporal LAI dynamics when the surface reflectance is absent for a long period owing to persistent cloud/aerosol contaminations. The results indicate that the new Bi-LSTM deep learning model runs significantly faster than the GLASS V5 algorithm, avoids the reconstruction of surface reflectance data, and is resistant to the noises (cloud and snow contamination) or missing values contained in surface reflectance than other methods, as the Bi-LSTM can effectively extract information across the entire time series of surface reflectance rather than a single time point. To our knowledge, this is the first global time-series LAI product at the 250-m spatial resolution that is freely available to the public (www.geodata.cn and www.glass.umd.edu).

1. Introduction

Leaf area index (LAI) is one of the terrestrial essential climate variables designated by the Global Climate Observing System (GCOS) and is widely used in a variety of scientific applications, including terrestrial ecosystem model simulation, crop yield estimation, and vegetation change monitoring. There are two typical definitions of LAI: the true LAI, which is described as half of the total green leaf area per unit of the horizontal land surface (Chen and Black, 1992; Yan et al., 2019), and the effective LAI, which assumes the random distribution of leaves and represents the product of the true LAI and the clumping index (i.e., the degree of foliage distribution relative to a random one) (He et al., 2012).

Satellite observation data have provided the only reliable means for global time-series mapping of LAI. Current global LAI products are estimated from various satellite data (Fang et al., 2019a; Liang and Wang, 2019), such as the Advanced Very High-Resolution Radiometer (AVHRR), Moderate Resolution Imaging Spectroradiometer (MODIS), and SPOT/VEGETATION. The retrieval algorithms of these LAI products are mainly based on physical or statistical methods. Physical methods are based on LAI inversion from radiative transfer models in different

* Corresponding author.
E-mail address: sliang@umd.edu (S. Liang).

https://doi.org/10.1016/j.rse.2022.112985
Received 4 July 2021; Received in revised form 23 February 2022; Accepted 2 March 2022
Available online 10 March 2022

fashions. For example, MODIS LAI is generated using look-up-tables (LUTs) created from a three-dimensional (3D) radiative transfer model (Myneni et al., 2002), CYCLOPES LAI is produced using artificial neural networks (ANNs) trained from the PROSAIL model (Baret et al., 2007), and the GLOBCARBON LAI is based on a four-scale model (Feng et al., 2006). Statistical methods are based on statistical relationships between LAI and surface reflectance, or vegetation indexes. For example, GEOV LAI is developed from the CYCLOPES and MODIS LAI using the heuristic arguments fusion method and ANN model (Baret et al., 2013); The Global LAnd Surface Satellite (GLASS) LAI is trained from the fused time-series LAI from the CYCLOPES and MODIS LAI products and the reprocessed MODIS red and near-infrared surface reflectance (Liang et al., 2021; Xiao et al., 2014); GLOBMAP LAI is derived from the empirical relationship between AVHRR normalized difference vegetation index (NDVI) and MODIS LAI (Liu et al., 2012); a recent study by Kang et al. (2021) mapped 30-m LAI for the contiguous US by building a relationship between Landsat reflectance and MODIS LAI product using the random forest model.

However, there are several issues in generating global LAI products. First, both estimation methods are sensitive to "noises" of the input surface reflectance, which is often contaminated by clouds or high-concentration aerosols, resulting in fluctuations or gaps in LAI time-series products. According to Yan et al. (2016b), the annual missing data rate of MODIS LAI can reach 40% in cloud- and snow-dominated areas and data gaps often occur in winter. It has been recognized that the temporal information contained in satellite observations must be fully utilized to generate spatiotemporal continuous data products. GLASS LAI was produced in this context by exploiting multi-temporal satellite data using a general regression neural network (GRNN). Although the GLASS LAI algorithm reconstructs the continuous surface reflectance using a vegetation indices based smoothing method (Xiao et al., 2015), the current version (V5) product still has many abnormal values and unrealistic seasonality in winter in middle- and high-latitude areas (Section 5). Besides, the surface reflectance reconstruction process for GLASS LAI is extremely time-consuming because of the optimization process for searching for the minimum of the cost function.

Second, current global LAI products have significant discrepancies owing to different input observation data and/or retrieval algorithms used. For example, the mean LAI difference between different products can be one unit in tropical forest areas (Yan et al., 2016b), which may cause substantial uncertainties in vegetation change analysis and land surface model simulations (Alkama et al., 2022; Jiang et al., 2017; Piao et al., 2015). This calls for the exploration of various estimation methods to produce more accurate global LAI products.

Third, the Global Observing System for Climate (GCOS) requires LAI product to have a spatial resolution of 250 m for carbon modeling (GCOS, 2016); however, current LAI products cannot meet such a requirement, except those that are either regional or as short as one year, such as the University of Toronto LAI product from MODIS data (Gonsamo and Chen, 2014). The PROBA-V global LAI product at 300-m resolution and 10-day frequency is close to the GCOS requirement; however, the temporal span is only from 2014 to 2020. MODIS provides the only long time-series data source with a spatial resolution of 250 m beginning from 2000, there is an urgent need to produce a long time-series global LAI product with higher accuracy and finer spatial resolutions from MODIS data.

Most estimation algorithms use multiple bands of satellite data, but few also exploit temporal signatures, which can potentially help resolve some of the issues identified above. Taking full advantage of signatures in both the spectral and temporal dimensions in satellite observations requires a more robust time-series modeling method that can learn much more from data than traditional machine learning models, which have a shallow architecture. With the increasing satellite data availability and computing power in recent years (Ball et al., 2017), deep learning has succeeded and outperformed traditional machine learning models in various remote sensing estimation applications, such as estimating soil moisture (Fang et al., 2019b), precipitation (Wu et al., 2020), land surface and air temperature (Shen et al., 2020; Svendsen et al., 2020), and crop yield (Jiang et al., 2020). Among the numerous deep learning architectures, the recurrent neural network (RNN) can address the temporal dependencies in time-series data (Sherstinsky, 2020) and deal with time-series regression or forecasting of satellite data (Yuan et al., 2020). The variants of RNN include the long short-term memory (LSTM) network (Hochreiter and Schmidhuber, 1997), the gated recurrent unit (GRU) (Cho et al., 2014), and the bi-directional LSTM (Bi-LSTM) (Huang et al., 2015), which were developed to address the limitation of RNN in learning long-term temporal dependencies.

This study aims to explore the deep learning approach for generating a new version (V6) of GLASS LAI product at the 250-m resolution from MODIS surface reflectance data. GLASS LAI product has been widely used (Liang et al., 2021), but the current version (V5) has several limitations, such as temporal fluctuation, data gaps, high dependence on the quality of surface reflectance, and low production efficiency. This new V6 GLASS LAI is designed to effectively address these issues and also increase the spatial resolution from 500 m to 250 m.

The structure of the remainder of this article is as follows. Section 2 describes the methodology for generating the V6 LAI product, Section 3 introduces the data employed, Section 4 presents the results analysis, and the discussion and conclusion are given in Sections 5 and 6, respectively.

2. Methods

The GLASS V6 LAI algorithm is based on the deep learning approach. There are several key issues addressed by the algorithm, among which are the creation of time-series training data and the selection of a deep learning model. As there is no in situ measured time-series LAI dataset that is large enough to be used as "true values" for model development, our strategy for determining the "true values" is to identify the pixels with the closest values in the three "best" global LAI products, namely, MODIS Collection 6, GLASS V5, and PROBA-V V1 LAI, which have the same LAI definition (true LAI). The assumption is that if three products have very close values for a specific pixel, the average/median of these three values may better represent the actual LAI value of that pixel. The LAI values of the identified pixels and the corresponding band combinations of MODIS 8-day surface reflectance (MOD09A1) at 500 m constitute the global samples for model training and validation. To build the relationship between time-series LAI and reflectance, four machine learning models, GRNN, LSTM, GRU, and Bi-LSTM, are evaluated to identify the best model for product generation.

The schematic overview of this algorithm is illustrated in Fig. 1 and contains five key steps:1) creation of training samples that are globally distributed and representative of major land-cover types; 2) determination of the best deep learning model by exploring four models; 3) generation of the primary LAI products at 500-m and 250-m resolutions by implementing the trained models to six-band 500-m and two-band 250-m surface reflectance, respectively; 4) consolidation of the primary LAI estimates at a 250-m and 500-m resolution using the temporal and spatial weighted average; because the 500-m estimates are based on six surface reflectance bands with a higher modeling accuracy, the 250-m estimates from two bands are adjusted accordingly; and 5) validation of the new V6 GLASS LAI product using in situ measurements and intercomparison with the existing products. The details are described in the following subsections.

2.1. Creation of global training samples

Sufficient and representative training samples are the prerequisite of any deep learning model for remote sensing retrieval (Yuan et al., 2020). Our sampling strategy is to select global large samples of different vegetation types over different latitudes by ensuring that they have adequate temporal variations and also represent "true values".

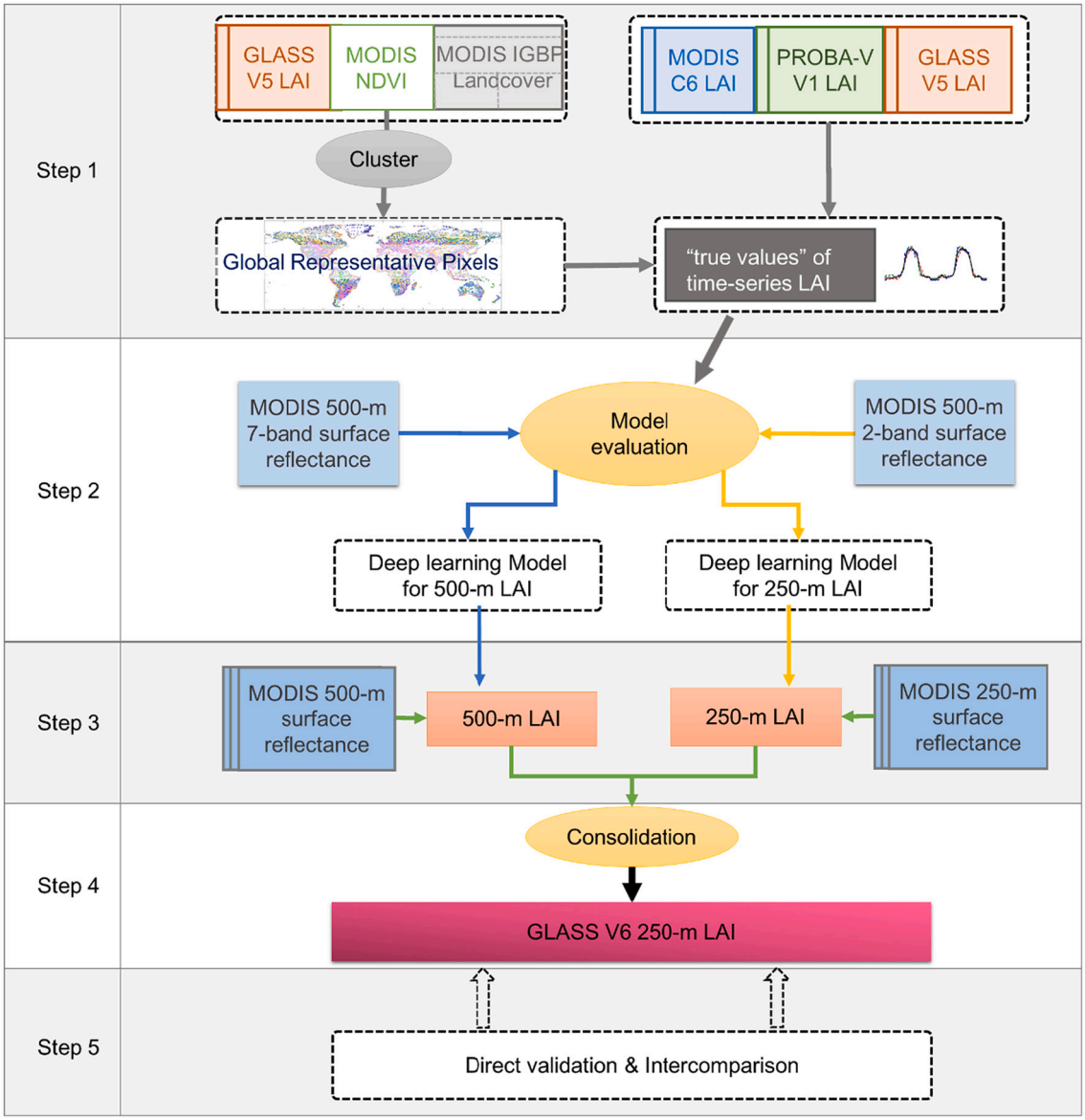

Fig. 1. GLASS 250-m LAI product (version 6) algorithm flowchart.

First, to reduce data redundancy and ensure adequate temporal variations, different types of the LAI temporal curves are identified by adopting the K-means clustering analysis of the GLASS V5 LAI and MODIS NDVI time-series curves sampled in the year 2014. Time-series GLASS LAI can indicate the vegetation seasonal variations, while NDVI can indicate whether the reflectance is contaminated by the cloud to some extent, based on the fact that cloud-contaminated NDVI usually shows lower values than NDVI under clear-sky conditions (Holben, 1986). Each MODIS land-cover type is clustered separately. The optimal number (k) of clusters is solved using the Calinski–Harabasz index (Caliński and Harabasz, 1974), which is defined as the ratio of the overall between-cluster and within-cluster variances with respect to k. After this procedure, a total of 40,712 clusters are generated. Basically, one cluster corresponds to one type with its unique seasonal change of LAI and the satellite observation condition.

To ensure each cluster represents the "true" LAI time-series, three LAI products (GLASS V5, MODIS C6, and PROBA-V V1) are compared to generate the representing LAI curves for a temporal sampling of 2 years (2014 and 2015, 92 time steps (one time step corresponds to 8-day)) over the whole growing season in both the northern and southern hemispheres. For land types of permanent snow and barren, we set MODIS LAI to 0 to avoid invalid values, and the same setting is applied to GLASS and PROBA-V LAI when they contain invalid values. For other land cover types, the percentage when three products all fail to provide a valid LAI within a year is extremely small, about 3.7×10^{-6}, and also about 70% of these pixels have corresponding NDVI values smaller than 0.2. As the Bi-LSTM model tolerates the noises in the samples, the LAI values of these data are also set to 0. For each pixel in each cluster, its mean square error (MSE) among these three LAI products is calculated as

$$MSE = \sum_{t=1}^{92}[MSE(GLASS_t, MODIS_t) + MSE(GLASS_t, PROBAV_t) + MSE(PROBAV_t, MODIS_t)] \quad (1)$$

where t is the time step.

As the quality control (QC) information contained in MOD09A1 product cannot help users identify cloud-sky conditions, the QC layer contained in MODIS LAI is used instead to calculate the percentage of high-quality LAI retrievals (HQ), which is similar to the percentage of

yearly clear-sky days in MOD09A1 data. We take MODIS LAI using the main algorithm with or without saturation as high-quality data (QC < 64). For each cluster, four pixels with the least MSEs and different HQ ranges (30%, 50%, 80%, and 100%) are selected to represent this cluster. As the MODIS LAI product is generated without pre- or post-processing of the cloud contaminated pixels and fluctuates more than GLASS and PROBA-V LAI, at each time step of the 2-year length, the average of GLASS and PROBA-V LAI is taken as the LAI value of the sample pixel if their difference is smaller than one unit, or the median value of MODIS, GLASS, and PROBA-V LAI is taken. If both MODIS and PROBA-V LAI are invalid at a time step, the GLASS LAI is taken. After the above procedure for each land cover type is performed, each 4° × 4° window is checked, and if no representative LAI curve is selected in the window, one LAI curve is added according to the above criteria. At last, a total of 52,997 representative LAI curves are created.

2.2. Selection of the deep learning model

2.2.1. Networks

To learn the temporal relationships between the MODIS surface reflectance and LAI, we evaluate four machine learning architectures that can interpret the temporal features in data, including GRNN, LSTM, GRU, and Bi-LSTM.

1) *GRNN*

GRNN is a feed-forward neural network that can estimate continuous variables using nonparametric estimators of the probability density function (Specht, 1991). It is known for its effective fitting ability for sparse datasets. There is no iterative process in training GRNN, but the free smoothing parameter (σ) needs to be estimated. GRNN consists of four layers: input, hidden, summation, and output (Fig. 2a). The neurons contained in the first three layers are fully connected, while the neurons in the summation layer are divided into the summation neurons and a division neuron. GRNN is used in the previous GLASS LAI algorithm (Xiao et al., 2014) for training the model between the fused MODIS and CYCLOPES LAI with reprocessed MODIS surface reflectance by adopting a holdout method to estimate the smoothing parameter.

2) *LSTM, GRU, and Bidirectional LSTM*

One problem in the feedforward network is in characterizing the sequence features with gaps in variables. The RNN, which can learn to process sequence data using the internal memory state recursively, has become a solution (Thireou and Reczko, 2007). As improved variants of RNN architecture, LSTM and GRU networks can address the exploding and vanishing gradient problem of RNN (Cho et al., 2014; Hochreiter

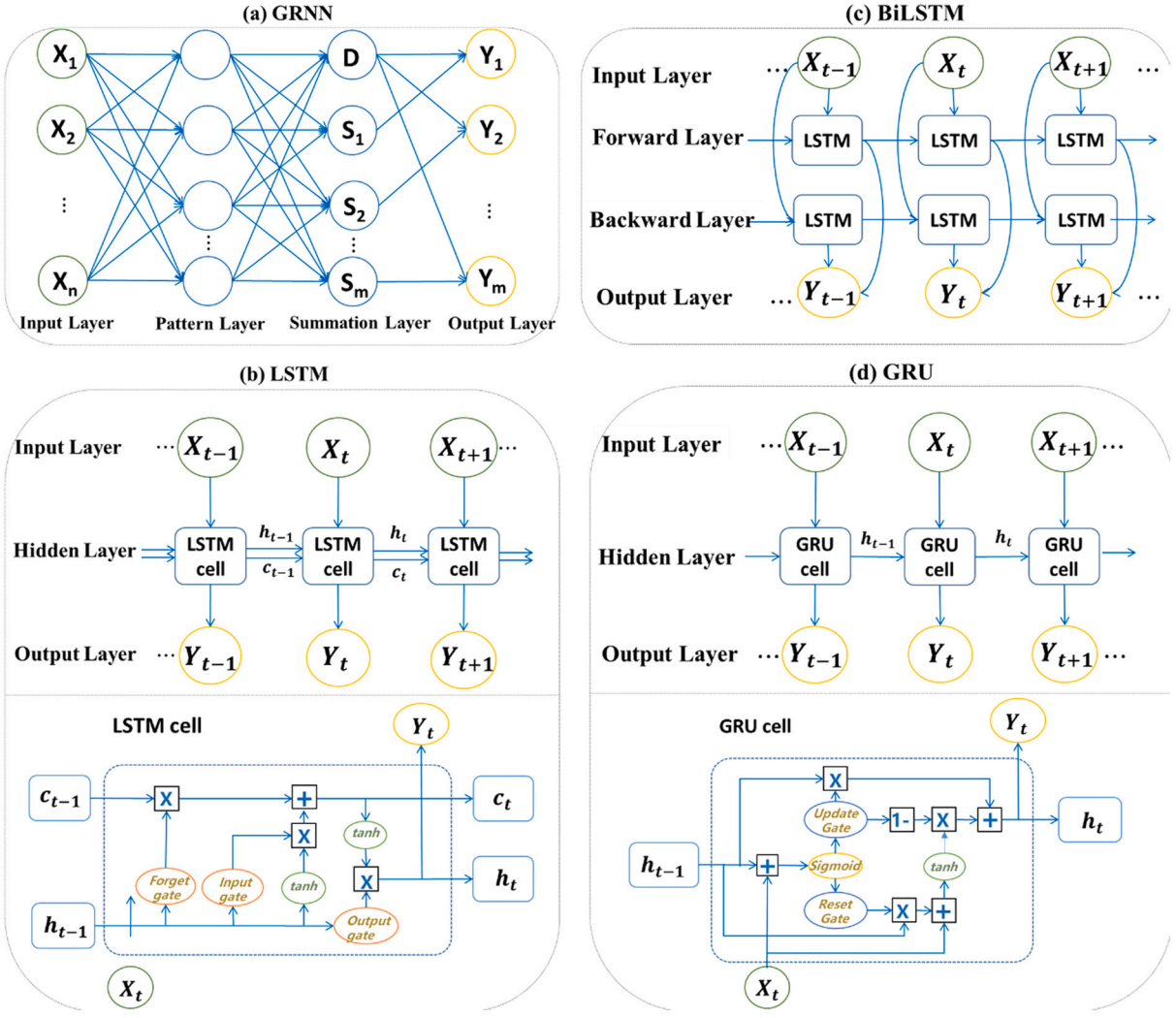

Fig. 2. Structures of the four deep learning models adopted in this study: (a) GRNN: X is the time series of surface reflectance, n is the number of samples, Y is LAI, and m is the time series length of LAI; (b) LSTM; (c) Bi-LSTM; (d) GRU. In subplots (b-d), X_t and Y_t is the surface reflectance and LAI at time step t, respectively, and h_t and c_t are the hidden state and current state at time step t, respectively.

and Schmidhuber, 1997). An LSTM layer is composed of a set of memory cells that contain the input gate, output gate, and forget gate. The cell state can store long-term information, and the three gates can modulate the flow of information. The key feature of LSTM is that these memory cells can selectively keep or discard relevant information at each time step (Yildirim, 2018). Fig. 2b shows the LSTM architecture and its inner cell structure. During a forward pass, the previous cell state (c_{t-1}) is first regulated by the forget gate using the current input (X_t) and previous output hidden state (h_{t-1}); then, the current cell state (c_t) is computed using the activation value of the input gate and previous memory; at last, the output of the cell (h_t) is derived by multiplying the activation of the output gate. The forget gate determines the amount of the previous information to keep while the input gate decides which new information to be added.

The GRU is a variant of LSTM that has fewer parameters and superior speed compared to LSTM. The structure of GRU and its inner workings is shown in Fig. 2d, where only the hidden state passes between time steps. The update gate and reset gate are the only two gates inside the GRU cell, which are derived from the previous hidden state and current input, and they control the extent of the previous state to be retained and new information to be added to derive the current hidden state.

The Bi-LSTM is another alternative RNN containing two separate recurrent net layers: the forward and backward layers (Graves and Schmidhuber, 2005). As shown in Fig. 2c, these two layers are connected to each other, and both are connected to the output layer; with such a structure, Bi-LSTM can learn both the previous and future information of the time series at each time step.

2.2.2. Datasets for model training

The corresponding 2014–2015 time-series MODIS surface reflectance data at the representing pixels are extracted as the control variables, and the fused time-series LAI from MODIS, PROBA-V, and GLASS LAI (see Section 2.1) is the target variable. The samples are randomly divided into three groups, namely, the training dataset used to obtain a deep learning model (70%), the validation dataset used to select the optimal model (20%), and the test dataset used for evaluating the final model (10%).

2.2.3. Model training

At first, different machine learning models are evaluated to choose the most suitable model for LAI estimation. To reduce model complexity and save training time, only 1-year time-series LAI data in 2014, the first two red and near-infrared bands (b1, b2) at central wavelengths of 645 and 858 nm, and three angles (solar zenith, view zenith, and relative azimuth angles) of MODIS surface reflectance are used for training. The four machine learning models are implemented using the deep learning toolbox in MATLAB (version 2020a). For the GRNN model training, we use the same procedure as in the previous GLASS LAI algorithm, except we use the updated training samples and keep the original surface reflectance data without reprocessing. For the three deep learning models (LSTM, GRU, and Bi-LSTM), they are designed as one input layer, one LSTM/GRU/ Bi-LSTM layer with 200 nerus, one dropout layer, and one regression layer; we keep the same training algorithm and parameters, using the Adam optimizer, an initial learning rate of 0.0001, a batch size of 100, and max epochs of 100. However, different training methods are likely better suited to different models.

Then, the time-series length is investigated to determine the optimal temporal length on the best-performing model. Training data with 23 different temporal lengths from 32 days to 2 years (32-day time interval) are used in this evaluation. After that, different combinations of the MODIS surface reflectance bands with a temporal length of 1 year are further evaluated in selecting suitable feature sets for the deep learning model. The three solar and viewing angles (solar zenith, view zenith, and relative azimuth angles), as well as the first two bands of MODIS surface reflectance, are first explored as the basic combination, and other bands are added successively. Finally, we retrain the selected deep learning model using the suitable feature sets and temporal length to determine the final 500-m LAI estimation model. As the MODIS 250-m surface reflectance has only two bands (b1, b2), the 250-m LAI model is finally retrained using the selected deep learning model with the optimal temporal length and the basic band combination.

2.3. Estimating LAI at 250-m and 500-m resolutions

We first use the best trained model along with the time-series MODIS surface reflectance data to estimate global time-series LAI, with a spatial resolution of 500 m and a time frequency of 8 days. It takes about 24 h to produce 2 years' global 500-m LAI data on a single GPU, which is about 10 times faster than generating the GLASS V5 LAI product.

Because of the training error of the model, the derived LAI time series at two successive time windows of the optimal temporal length is not necessarily continuous. According to the model evaluation result (Section 4.2), the optimal temporal length of the time series is 2 years (92 time steps (t)). Similar post-processing of the previous GLASS algorithm is adopted here (Xiao et al., 2014). We calculate the time-series LAI twice, with a time shift of half of the time-series length (1 year), and multiply a weight function by the two time-series LAI to derive the final estimate (Eq. (3)). The weight function (w) is also adopted from the previous GLASS algorithm and updated as follows:

$$w = \begin{cases} 0 \quad (1 \le t \le 4) \\ 0.5*\left(cos\left(\frac{-\pi*t}{37}+\frac{\pi*42}{37}\right)+1\right) \quad (5 \le t \le 42) \\ 1 \quad (43 \le t \le 50) \\ 0.5*cos\left(\frac{\pi*t}{37}-\frac{\pi*51}{37}\right)+1\Big) \quad (51 \le t \le 88) \\ 0 \quad (89 \le t \le 92) \end{cases} \tag{2}$$

and the LAI at time step (t) for the current year (LAI_t) is calculated as

$$LAI_t = LAI1_{t+46} \bullet w_{t+46} + LAI2_t \bullet w_t \ (1 \le t \le 46) \tag{3}$$

where $LAI1$ is the time-series LAI for the previous and current year, and $LAI2$ is the time-series LAI for the current and following year.

The 250-m LAI model is executed with 250-m surface reflectance to estimate the global 250-m, 8-day LAI. The computation time for the 250-m LAI product is nearly twice that of the 500-m product, as the number of pixels has increased fourfold, while the 250-m model computational speed for a pixel is slightly higher (14%) than the 500-m model, and the 250-m time-series data only needs to be calculated once, because the next consolidation procedure ensures the its spatiotemporal consistence with the 500-m data.

2.4. Consolidation of 250-m and 500-m estimates

The 500-m estimates from the six-band surface reflectance are more accurate than the 250-m estimates with two bands, according to the evaluation results (Section 4.2). To maintain their consistency, we apply a post-processing procedure to the 250-m estimates. Within each 500-m pixel, the four 250-m pixels ($LAI250_i$) are normalized to match the 500-m value ($LAI500$):

$$\begin{pmatrix} \widetilde{LAI250}_1 & \widetilde{LAI250}_2 \\ \widetilde{LAI250}_3 & \widetilde{LAI250}_4 \end{pmatrix} = \begin{pmatrix} LAI250_1 & LAI250_2 \\ LAI250_3 & LAI250_4 \end{pmatrix} \times \frac{4 \cdot LAI500}{\sum_1^4 LAI250_i} \tag{4}$$

where $\widetilde{LAI250}_i$ represents the normalized 250-m LAI values.

Finally, the spatiotemporal continuous GLASS LAI (version 6.0)

product is generated, with a time span from 2000 to 2020, a frequency of 8 days, and two spatial resolutions of 500 m and 250 m.

2.5. Evaluation of the GLASS V6 LAI product

The GLASS V6 LAI products are evaluated using two widely used approaches for remote sensing product validation (Justice et al., 2000; Wu et al., 2019). First, they are directly validated using ground datasets, including the LAI reference maps regressed from field measurements and high-resolution satellite data, and ground LAI datasets representative of 3-km collected from several ground observation networks. The accuracies of GLASS V6 LAI are quantified at the 250-m, 500-m, and 3-km resolution scales. Five metrics are used in the validation: number of samples points (N), R^2, RMSE, bias, and the percentage of pixels meeting the target accuracy requirement (P).

Second, they are inter-compared with the existing LAI products, and the spatial continuity is assessed at the global scale using the mean LAI in January and July of 2018. The temporal consistency is also analyzed at eight typical sites with different biome types. At last, the global LAI trend from 2000 to 2018 is analyzed. The LAI products are first aggregated to 0.05° at their original temporal resolutions, and the annual average LAI of MODIS, PROBA-V, GLASS V5, and V6 products are calculated for the land surface between 70° N and − 60°S. The same quality filter criterion is applied for GLASS V5, V6, and PROBA-V products (pixels with LAI $>$ 7 and water pixels are filtered out). As for MODIS LAI, pixels with a low QC indicator or meeting the above criterion are filtered out. For a fair comparison, land-cover types of permanent snow/ice and barren are set to zero for each product.

3. Data

3.1. Satellite products

A total of six global satellite products are used in this study, namely, the MODIS LAI, GLASS LAI, PROBA-V LAI, MODIS 250-m and 500-m surface reflectance, and MODIS land-cover type products. The three LAI products are used to construct the time-series LAI samples, while the surface reflectance and land-cover type products are used to train the deep learning model as well as to produce global LAI data.

1) *MODIS LAI (MCD15A2H, V6)*

MODIS LAI is defined as true LAI and accounts for clumping at the plant scale. The Terra+Aqua MODIS LAI product is produced based on biome-specific LUTs generated from a three-dimensional radiative transfer model; also, a backup solution that links the Normalized Difference Vegetation Index (NDVI) to LAI is activated when the main algorithm fails. After the daily LAI is retrieved from MODIS daily red and near-infrared (NIR) surface reflectance, temporal compositing and quality control are applied to generate the 8-day product (Myneni et al., 2015; Myneni et al., 2002; Yan et al., 2016a). Evaluation of the Collection 6 MODIS LAI shows that it agrees well with the field LAI measurement. Besides, it can capture the seasonality of different biomes, except for the evergreen broadleaf forest (EBF), owing to the lack of high-quality satellite observations (Yan et al., 2016b).

2) *PROBA-V LAI (V1)*

The PROBA-V LAI (V1) of CGLS (Copernicus Global Land Service) is produced using an artificial neural network (ANN) from the PROBA-V red and NIR surface reflectance (Baret et al., 2016b). The ANN is trained from the weighted average of V3.1 CYCLOPES and the Collection 5 MODIS LAI product. Then, temporal compositing, filtering, and gap filling are applied to the instantaneous LAI estimates by ANN, discriminating between EBF and no-EBF pixels. Note that CYCLOPES LAI is defined as effective LAI and only accounts for clumping at the landscape scale. However, as pointed out by Baret et al. (2013), for lower LAI values, clumping described at the plant level in MODIS approximates clumping at the landscape scale in CYCLOPES; for higher LAI values, the fused LAI preserves the clumping at the plant scale using the heuristic arguments method. Therefore, PROBA-V LAI is deemed as true LAI. Recent validation of the PROBA-V LAI product revealed that PROBA-V LAI agreed better with ground reference data from 20 NEON sites than MODIS LAI and VIIRS LAI products; besides, this product also showed smoother temporal profiles compared to the MODIS LAI product (Brown et al., 2020; Fuster et al., 2020).

3) *GLASS LAI (V5)*

GLASS V5 LAI is produced from MODIS surface reflectance data through a GRNN, which is trained from the fused time-series LAI from the CYCLOPES and MODIS LAI and the reconstructed MODIS red and NIR surface reflectance (Liang et al., 2021; Xiao et al., 2014). As the CYCLOPES LAI is converted to true LAI using POLDER derived clumping index product (Chen et al., 2005) before fusing with MODIS LAI, the definition of GLASS LAI is also true LAI. Several validation studies have demonstrated its high accuracy among long-term, coarse-resolution LAI products (Jin et al., 2017; Li et al., 2018; Xu et al., 2018). The main characteristic of GLASS LAI is its temporal and spatial continuity and its smooth temporal profiles, which stem from the reprocessing of the input surface reflectance (Liang et al., 2021).

The basic characteristics of the three LAI products are given in Table 1. Note that these three LAI products are defined as the true LAI. Two-year LAI products in 2014 and 2015 are used to create the global training samples. For creating the LAI training samples, simple quality control is performed on the three LAI products: LAI outside [0, 7] range is set as invalid values, as the maximum physical value of moderate-resolution LAI is 7 (Baret et al., 2016a). For product evaluation and inter-comparison, the MODIS LAI pixels with QC $\geq$ 64 are filtered out.

4) *MODIS surface reflectance product (MOD09A1, MOD09Q1, V6)*

Seven visible, near-infrared, and shortwave surface reflectance bands, as well as the sun illumination and satellite viewing geometry information (solar zenith angle θ_s, view zenith angle θ_v, and relative azimuth angle φ) provided by MOD09A1 product are used as the primary input datasets of this algorithm. The central wavelengths of the seven MODIS surface reflectance bands (b1, b2…b7) are at 645, 858, 469, 555, 1240, 1640, and 2130 nm, respectively. Besides, the 250-m red and NIR reflectance provided by MOD09Q1 are also used to produce the 250-m LAI.

Note that although the MODIS surface reflectance has been atmospherically corrected for gases, aerosols, and Rayleigh scattering, residual noise caused by clouds still exists. Unlike previous GLASS LAI algorithms, the surface reflectance is not smoothed in this deep learning framework; during model training and LAI production, the MODIS surface reflectance data (including reflectances and angles) is specified as zero when it has reflectance value that exceeds the range [01], or when the solar zenith angle is larger than 85°, where atmospheric correction is not applicable (Vermote and Ray, 2015).

5) *MODIS land-cover product (MCD12Q1, V6)*

The 500-m static MODIS land-cover product in 2014 is employed to classify the GLASS LAI and MODIS NDVI pixels into different land-cover types, for further clustering of the LAI for each International Geosphere-Biosphere Program (IGBP) land-cover type (Sulla-Menashe and Friedl, 2018). The IGBP land-cover classification scheme has 16 classes, including 11 natural vegetation types (evergreen needleleaf forests (ENF), evergreen broadleaf forests (EBF), deciduous needleleaf forests (DNF), deciduous broadleaf forests (DBF), mixed forests (MF), closed shrublands (CSH), open shrublands (OSH), woody savannas (WSA),

Table 1
Characteristics of the satellite products used in this study.

Product (version)	Spatial resolution	Temporal resolution	Timespan used in model development	Timespan used in LAI production	Data provider
MODIS LAI (MCD15A2H V6)	500 m	8 days	2014, 2015	–	NASA
GLASS LAI (V5)	500 m	8 days	2014, 2015	–	BNU
PROBA-V LAI (V1)	300 m	10 days	2014, 2015	–	CGLS
MODIS surface reflectance (MOD09A1 V6)	500 m	8 days	2014, 2015	2000–present	NASA
MODIS surface reflectance (MOD09Q1 V6)	250 m	8 days	–	2000–present	NASA
MODIS land cover (MCD12Q1 V6)	500 m	yearly	2014	2000- present	NASA

savannas (SAV), grasslands (GRA), permanent wetlands (WET)), 3 developed and mosaic lands (croplands (CRO), urban and built-up lands (URB), cropland/natural vegetation mosaics (CVM)), and 2 non-vegetated lands (permanent snow and ice (SNO), and barren (BSV)).

Although the LAI, surface reflectance, and land-cover products are used for model development, the GLASS-V6 LAI production model inputs only include the MODIS surface reflectance time series and the associated angular information. In post-processing, water masks provided by MCD12Q1 are used for filtering out the water pixels.

3.2. Ground LAI reference data

To directly validate the generated LAI product against field measurements, we collect 79 available high-resolution LAI reference maps from 2000 to 2016 at 47 sites from Bigfoot (Gower and Kirschbaum, 2008), VALERI (Baret et al., 2021), and ImagineS (Fuster et al., 2020) networks with different dominant biome types (Table S1). The LAI reference maps are generated from local regressions between the LAI ground measurements and the high-resolution satellite reflectance (such as Landsat and SPOT) acquired around the ground campaign dates. Among the 79 maps, 18 maps that only provide effective LAI are converted into true LAI by dividing the corresponding clumping index, and as the field-measured or the Landsat/SPOT scale clumping index data are not available, the moderate-resolution clumping index product (He et al., 2012) is used here although the scale-mismatch error may be introduced. Next, we reproject the reference maps to MODIS sinusoidal projection and upscale them to 250-m and 500-m resolution to pair them with the LAI products. As the accuracy of the reference data may vary from site to site (Garrigues et al., 2008), a quality control process is applied using the relationship between NDVI and LAI (Kang et al., 2016) from the 79 maps. The NDVI is calculated from MODIS 500-m and 250-m surface reflectance data around the reference LAI date. With the assumption that there should be a positive correlation in NDVI and LAI, the NDVI-LAI points falling inside the 10%–90% percentile in each LAI bin (100 bins from 0 to 10, with a width of 0.1) are selected as high-quality data (Fig. S1).

Apart from the high-resolution reference LAI maps, the DIRECT dataset (http://calvalportal.ceos.org/web/olive/site-description), which is a collection of ground LAI measurements that can represent 3 × 3 km area of each site, is also used for validation of the LAI products at the 3-km scale.

4. Results

4.1. Global representative samples

A total of 52,997 global representing pixels are selected using the cluster analysis method described in Section 2.1, and their distribution is shown in Fig. 3, with 445 Benchmark Land Multisite Analysis and Intercomparison of Products (BELMAINIP) sites as references (Baret et al., 2006). The BELMAINIP network is designed to be representative of different land-surface types and conditions for evaluation of land biophysical products. BELMAINIP sites are taken as training samples for the previous version GLASS LAI algorithm. However, it has been reported that the northern mid-latitude surface is slightly over-representing, while the bare soil, grass, and evergreen broadleaf surfaces are under-representing by the BELMAINIP network (Baret et al., 2006).

The selected pixels are distributed in different continents and latitudes, covering each vegetation biome type. The number of samples for each biome is roughly proportional to the original IGBP land-cover surface area. Pixels at the bare land surfaces and snow-covered high

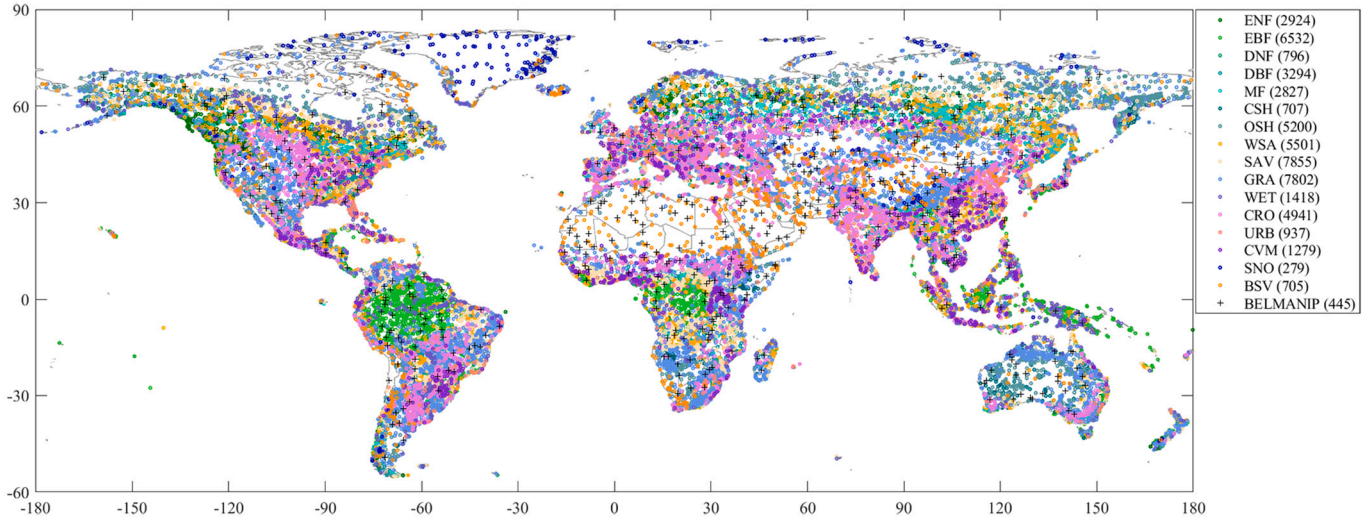

Fig. 3. Distribution of the representative pixels (the number of pixels for each land-cover type is shown in the legend).

latitude areas, such as the Sahara Desert and Greenland Island, are also included. To evaluate the representativeness of the fused LAI values of the selected pixels, histograms of the maximum, mean, and all of the LAI values of the 2014–2015 time series for the fused LAI at the selected pixels, as well as the GLASS V5, MODIS, and PROBA-V LAI at the global land pixels are shown in Fig. 4. For the maximum LAI, the fused LAI at the selected pixels is well distributed between [0, 6], although its frequency at the [6, 7] interval is lower, it is still between the distribution of the other three products at global land pixels (Fig. 4a). For the mean and all of the LAI values during 2014–2015, the distributions of the fused LAI samples are also similar to those of the three products at the global land pixels (Fig. 4b-c). The corresponding solar/satellite geometries of the MODIS data are further examined to avoid the extrapolation of the trained model. As shown in Fig. 4d-f, the distributions of the solar zenith, view zenith, and relative azimuth angles of the 2014–2015 MODIS reflectance data at the selected pixel are almost coincident with that of the global land pixels. The valid range of the solar zenith angle shown in Fig. 4d is [0, 85°]; therefore, the models trained using these samples can only output the valid LAI values when the solar zenith angle is within this range. The frequencies for the selected pixels at the four HQ ranges (30%, 50%, 80%, and 100%) are 0.014, 0.08, 0.22, and 0.69, respectively, which are similar to the frequencies of global LAI pixels (0.015, 0.11, 0.20, and 0.67), indicating that the samples are able to represent the different types of clear/cloudy satellite observation conditions within a year.

4.2. Evaluation of the models

The performance of the four machine learning models (GRNN, LSTM, GRU, and Bi-LSTM) in estimating time-series LAI is assessed using the training, validation, and test datasets using three metrics: the coefficient of determination (R^2), root mean square error (RMSE), and bias. According to Table 2, the GRNN achieves the lowest accuracy on both the validation and test datasets (RMSEs are about 1.2), which is expected as the time-series reflectance is not reconstructed, and the effects of cloud and snow contamination degrade the accuracy. Because of the similar control over temporal information flow, LSTM and GRU have similar performance levels on the three datasets. The highest accuracy is achieved by Bi-LSTM, which can be attributed to its unique ability in learning the bidirectional information contained in the temporal datasets.

The temporal length of the time-series data for the deep learning model was evaluated afterward. As shown in Fig. 5, the R^2 and RMSE on the training dataset tend to be constant earlier than for the validation and test dataset. The lowest RMSE is observed at a temporal length of 80, 84, and 88 for the training, validation, and test dataset, respectively. Considering the quality control of the fused time-series LAI, as well as the convenience for LAI production, we take 2 years (92 time steps) as the desirable temporal length.

To select the suitable feature sets for the selected Bi-LSTM model, we take the three solar and viewing angles, as well as the first two surface reflectance bands (red and near-infrared) as the basis, and added other bands successively according to their sensitivity to LAI. Based on the global sensitivity analysis (Saltelli et al., 2010) using simulations by PROSAIL, one of the most widely used canopy radiative transfer models (Jacquemoud et al., 2009), the sensitivity order for MODIS reflectance data is b7, b6, b5, b4, and b3. The evaluation results of the different band combinations are shown in Table 3. Generally, as the number of bands increases from 2 to 7, the RMSEs on the validation and the test datasets decrease and are closer to the training RMSEs. However, including band 5 makes no difference to the validation and test results, but reduces the training accuracy. Also, the improvement by including band 4 is limited for training and validation. Thus, we remove band 5 and band 4 successively. The accuracy on the three datasets improves

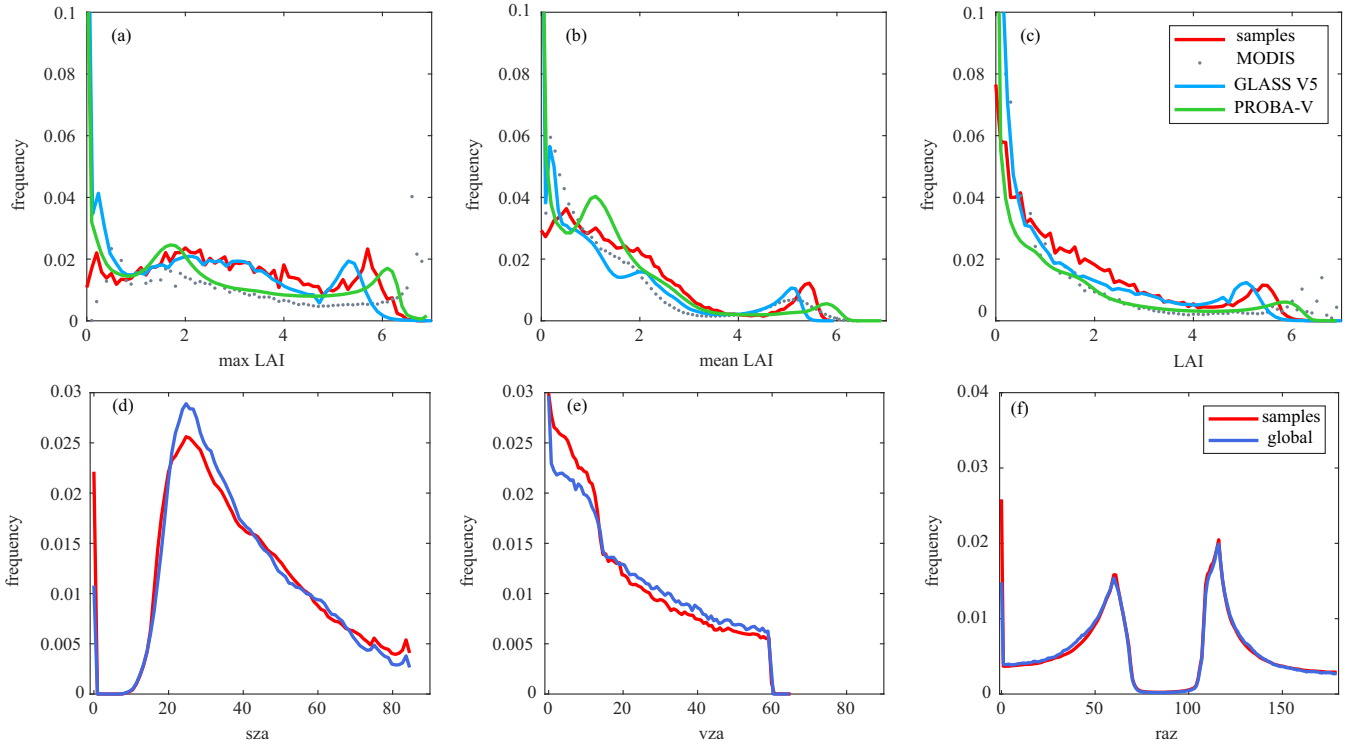

Fig. 4. Distribution of LAI values (bin width is 0.1) of the 2014–2015 time-series fused LAI samples at the representative pixels, and MODIS, PROBA-V, and GLASS V5 LAI at global land pixels: (a) "max LAI" represents the distribution of the maximum LAI values of the 2014–2015 LAI time-series, (b) "mean LAI" represents the distribution of the mean LAI values of the 2014–2015 LAI time-series, and (c) "LAI" represents the distribution of all the LAI values of the 2014–2015 time series; and distribution of (d) solar zenith, (e) view zenith and (f) relative azimuth angles (bin width is 1°) of the 2014–2015 time-series MODIS surface reflectance data at the representative pixels and the global land pixels.

Table 2
Evaluation of the different machine learning models using the training, validation, and test datasets.

	Training			Validation			Test		
	R^2	RMSE	Bias	R^2	RMSE	Bias	R^2	RMSE	Bias
GRNN	0.371	1.137	−0.18	0.335	1.262	−0.177	0.344	1.228	−0.161
LSTM	0.947	0.374	0.007	0.933	0.420	0.007	0.928	0.441	0.004
GRU	0.945	0.383	−0.019	0.930	0.431	−0.019	0.928	0.443	−0.021
Bi-LSTM	0.969	0.287	0.019	0.964	0.310	0.017	0.960	0.328	0.019

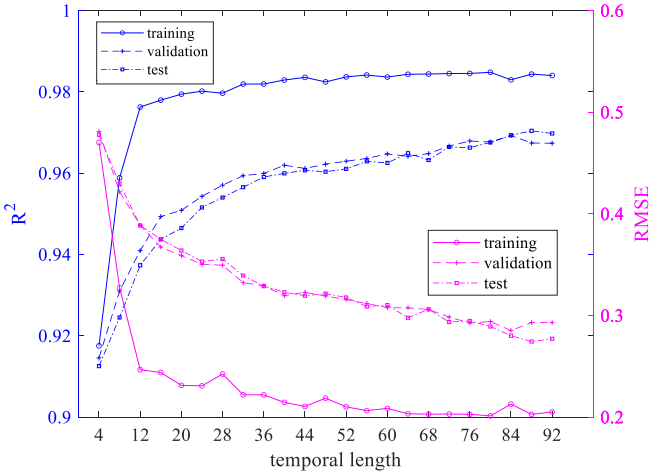

Fig. 5. Evaluation of temporal length in Bi-LSTM.

compared with the seven-band combination, and the best result is obtained using six bands without band 5. A previous study (Fang and Liang, 2003) reported that the combination of red and NIR bands performed best in estimating LAI from Landsat surface reflectance; however, this finding was based on the perfect atmospherically corrected images at a specific time. As we use time-series surface reflectance, in which noises inevitably exist, it is expected that adding more bands will aid in noise detection and removal when deriving temporal continuous LAI.

Therefore, the Bi-LSTM model, using the six MODIS bands without band 5, as well as three solar and viewing angles for a temporal length of 2 years with an 8-day interval as features (designated as the six-band model), is employed to produce the 500-m LAI. The 250-m LAI model adopts the same setting as the above 500-m model, except it uses the (b1, b2) band combination of MODIS surface reflectance as features (designated as the two-band model). The accuracy of the final retrained Bi-LSTM models for the 500-m and 250-m LAI is shown in the last two rows of Table 3, respectively.

4.3. Direct validation of LAI products

Direct validations of LAI products are performed at three scales: 250 m for PROBA-V at 300 m and GLASS V6 at 250 m; 500 m for MODIS, GLASS V5, and GLASS V6 500 m; and 3 km for all of them aggregated from their original resolutions.

Fig. 6a and b show the direct validation results of PROBA-V and GLASS V6 LAI product at the 250-m scale using 28 upscaled high-resolution LAI reference maps during 2014 to 2016 from ImagineS network. GLASS V6 and PROBA-V LAI have the same R^2 value (0.56); however, the RMSE and bias of GLASS V6 LAI are better than those of PROBA-V by about 0.16 and 0.06, respectively. By adding the remaining reference maps during 2000 to 2013, when PROBA-V LAI is not available, the R^2 of GLASS V6 improves to 0.67, while the RMSE is reduced to 0.92 (Fig. 6c). Although a small bias of −0.06 is observed, GLASS V6 250-m LAI shows underestimation at high values compared to the reference LAI maps.

Direct validation of MODIS, GLASS V5, and GLASS V6 500-m LAI product at the 500-m scale using 79 upscaled reference LAI maps are shown in Fig. 7. GLASS V6 achieves the highest accuracy (R^2 = 0.68, RMSE = 0.87), followed by MODIS (R^2 = 0.56, RMSE = 0.95) and GLASS V5 (R^2 = 0.53, RMSE = 1.08). MODIS LAI has fewer validation points than GLASS because of the missing data; besides, MODIS LAI is underestimated, with a bias of −0.28 at these sites. Fig. 8 shows the direct validation results of MODIS, GLASS V5, and GLASS V6 LAI products at the 3-km scale using the DIRECT dataset from 2000 to 2017. Most validation points are matched by GLASS V6 (N = 117). Consistent with the 500-m validation results, the highest accuracy is again achieved by GLASS V6 LAI (R^2 = 0.73, RMSE = 0.83). Note that in both Figs. 6 and 7, there are data points saturated around 5 for the GLASS V6 LAI, and they came from one forest site (HARV in Bigfoot). The field LAI ranges from 4.2–6.9 at this site on the validation date, while both GLASS V5 and V6 products are clustered from 5 to 5.8, although MODIS LAI contains data gaps and exhibits larger uncertainty, and its maximum value is 6.4. The time-series LAI of different products at this site is shown in Fig. 12c, the MODIS, GLASS V5, and V6 products have underestimated by about 0.5 compared to the LAI field data in 2000. GLASS V5 LAI has better accuracy than MODIS LAI at the 3-km scale, but its accuracy is lower at the 500-m scale, which may be because of the uncertainty introduced by its surface reflectance pre-processing procedure at the original 500-m scale,

Table 3
Evaluation of the different band combinations of MODIS surface reflectance in Bi-LSTM.*

	Training			Validation			Test		
	R^2	RMSE	bias	R^2	RMSE	bias	R^2	RMSE	bias
b1, b2	0.969	0.285	−0.006	0.961	0.322	−0.005	0.964	0.306	−0.009
b1, b2, b7	0.973	0.268	0.010	0.965	0.308	0.010	0.966	0.299	0.006
b1, b2, b6, b7	0.973	0.267	−0.005	0.965	0.306	−0.003	0.966	0.299	−0.006
b1, b2, b5, b6, b7	0.973	0.279	−0.025	0.965	0.306	−0.023	0.967	0.299	−0.028
b1, b2, b4, b5, b6, b7	0.971	0.279	−0.019	0.966	0.305	−0.019	0.966	0.299	−0.021
b1-b7	0.970	0.281	−0.024	0.966	0.301	−0.025	0.968	0.293	−0.026
b1, b2, b3, b4, b6, b7	0.971	0.278	−0.024	0.967	0.299	−0.024	0.968	0.291	−0.026
b1, b2, b3, b6, b7	0.971	0.279	0.021	0.966	0.301	0.020	0.967	0.292	0.019
Final six-band model (500 m)	0.980	0.230	0.009	0.972	0.271	0.011	0.973	0.266	0.011
Final two-band model (250 m)	0.980	0.228	0.011	0.968	0.290	0.012	0.969	0.283	0.010

* Each band combination includes three solar and viewing angle bands.

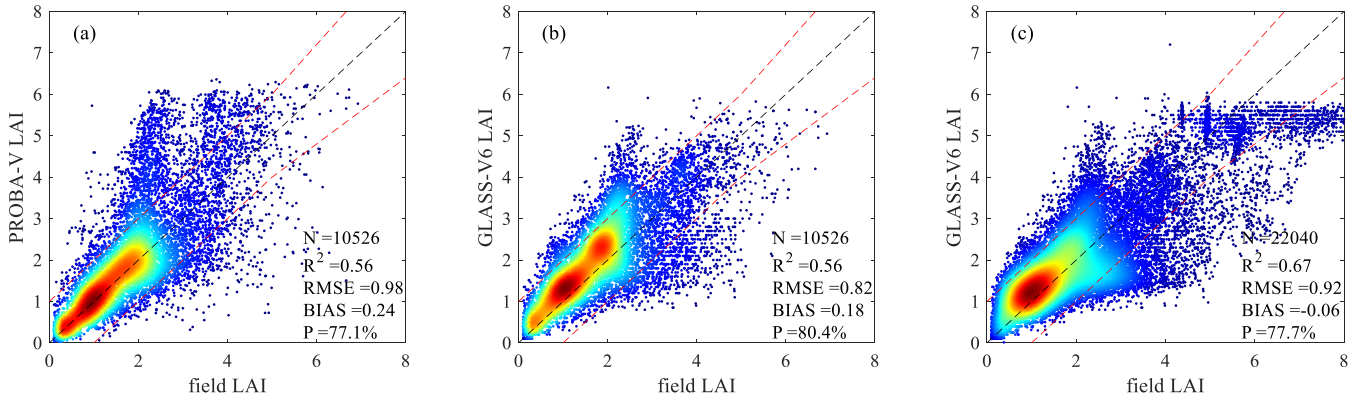

Fig. 6. Direct validation of (a) PROBA-V and (b) GLASS V6 LAI product at 250-m scale using 28 upscaled high-resolution LAI reference maps during 2014 to 2016 from ImagineS network; (c) direct validation of GLASS V6 LAI product at a 250-m scale using 79 high-resolution LAI reference maps during 2000 to 2016 from Bigfoot, VALERI, and ImagineS networks (red dashed lines represent the accuracy requirement, and P is the percentage of pixels meeting the accuracy requirement). (For interpretation of the references to colour in this figure legend, the reader is referred to the web version of this article.)

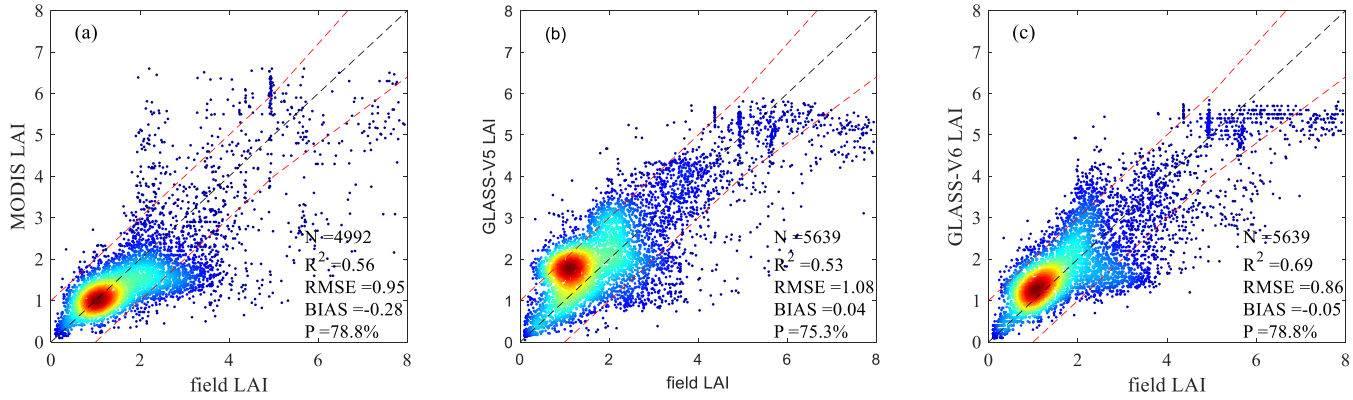

Fig. 7. Direct validation of (a) MODIS, (b) GLASS V5, and (c) GLASS V6 LAI product at a 500-m scale using 79 upscaled high-resolution LAI reference maps during 2000 to 2016 from Bigfoot, VALERI, and ImagineS networks (red dashed lines represent the accuracy requirement, and P is the percentage of pixels meeting the accuracy requirement). (For interpretation of the references to colour in this figure legend, the reader is referred to the web version of this article.)

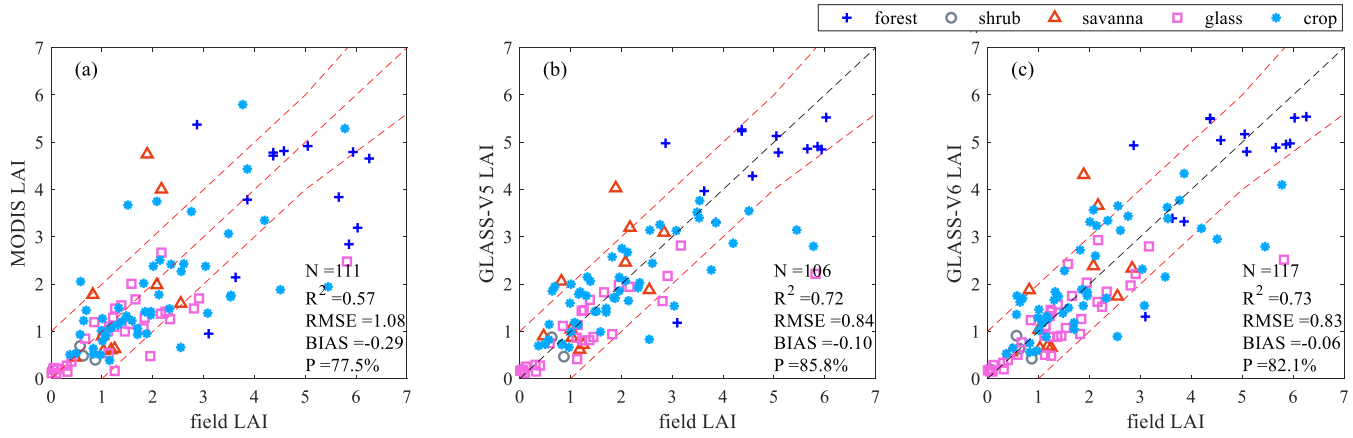

Fig. 8. Direct validation of (a) MODIS, (b) GLASS V5, and (c) GLASS V6 LAI product at a 3-km scale using the DIRECT ground measurement dataset during 2000 to 2017 (red dashed lines represent the accuracy requirement, and P is the percentage of pixels meeting the accuracy requirement). (For interpretation of the references to colour in this figure legend, the reader is referred to the web version of this article.)

and this error is spatially averaged when upscaling to 3-km; besides, GLASS V5 incorporated the 3-km field information in model training, while other products (including GLASS V6) are independent.

The accuracy of each product for different biome types is further explained at different scales, using the upscaled LAI reference maps and values during 2000 and 2017, except for PROBA-V (2014–2016). Results (Table S2) show that the uncertainties of GLASS V6 250 m and 500 m LAI are within the range of 0.77–1.13 for different biome types, while

the uncertainty ranges of GLASS V5 (0.81–1.71) and MODIS (0.83–1.7) are higher.

The target accuracy requirement of GCOS for the global LAI product is 15%; however, meeting this requirement remains a big challenge given the uncertainties of both field measurements and the regression based high-resolution LAI reference maps. Therefore, we use the same LAI requirement of 20% or 1 unit adopted by Brown et al. (2020) in evaluating the PROBA-V LAI product. According to the results in Fig. 6a and 6b, 77.1% PROBA-V 300-m LAI and 80.4% GLASS-V6 250-m LAI pixels are within the target accuracy at the ImagineS sites, while 77.7% GLASS-V6 250-m LAI pixels meet the requirement at the Bigfoot, VALERI, and ImagineS sites (Fig. 6c).

4.4. Spatial consistency analysis

The global distribution of the MODIS, PROB-V, GLASS V5 and V6 LAI in January and July of 2018 is shown in Fig. 9. The grey background in each subplot represents the vegetated land surface where the corresponding LAI product is unavailable. The biggest difference in these products is the spatial coverage. In July, MODIS and PROB-V LAI can provide valid LAI values up to 85°N. As introduced in Section 3.1, MODIS surface reflectance product is produced without atmospheric correction when the solar zenith angle is larger than 85° (Vermote and Ray, 2015), which roughly corresponds to 63°N at the beginning of the year. PROBA-V only filters out pixels when the solar zenith angle is

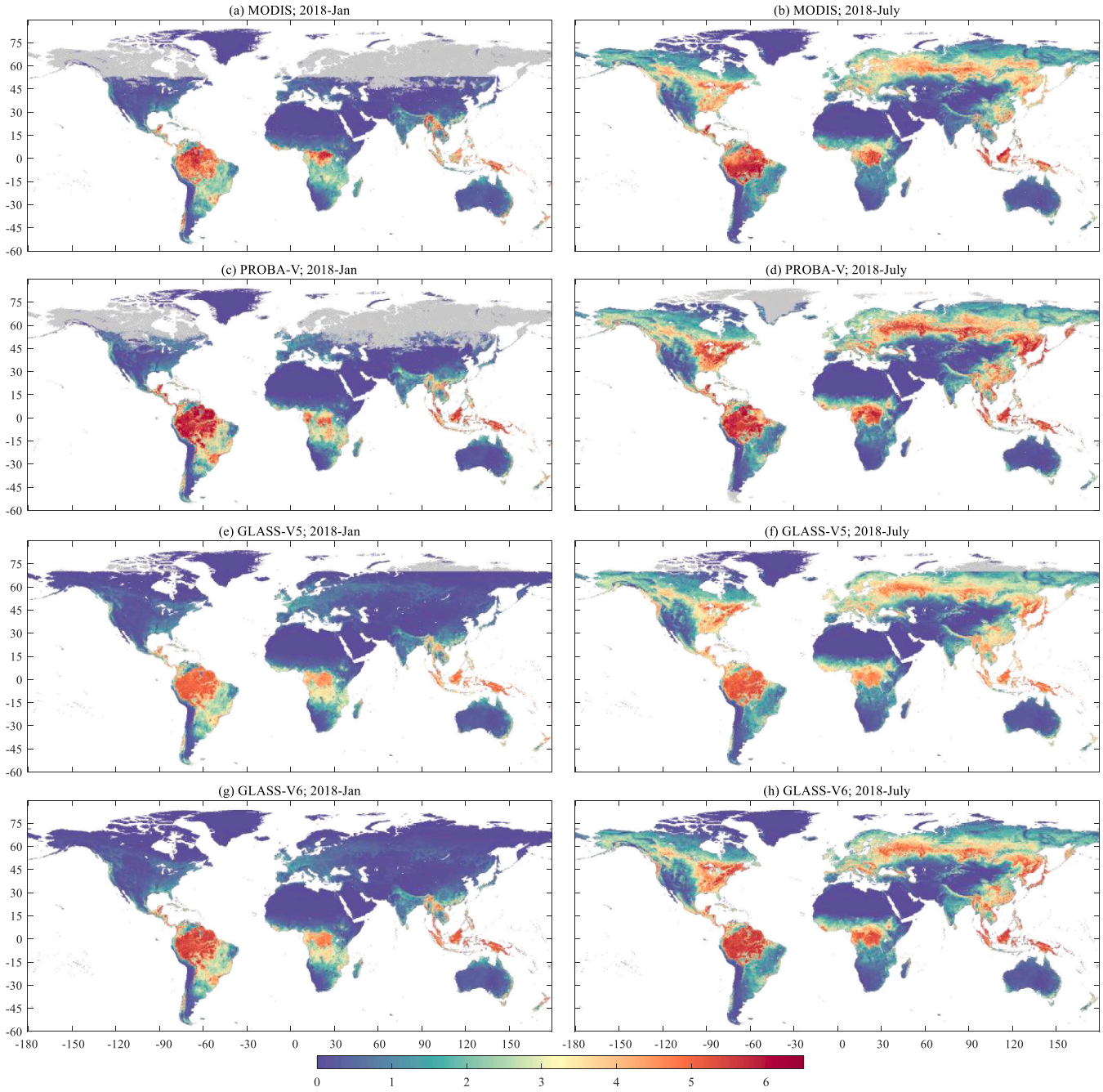

Fig. 9. Global distribution of the MODIS, PROB-V, GLASS V5, and V6 LAI in January and July 2018; the spatial resolution is 0.05 degree in geographic latitude/longitude; (a) MODIS, January 2018; (b) MODIS, July 2018; (c) PROBA-V, January 2018; (d) PROBA-V, July 2018; (e) GLASS V5, January 2018; (f) GLASS V5, July 2018; (g) GLASS V6, January 2018; and (h) GLASS V6, July 2018. MODIS, PROBA-V and GLASS-V5 LAI are set to 0 for the permanent snow and barren pixels when they do not provide values.

larger than 90°. Both MODIS and PROBA-V fail to provide LAI values above about 50°N in January, though they can provide valid LAI values at the large solar zenith angle (≤85°) based on global statistics of the distribution of the LAI products and MODIS solar zenith angle data within a year. Therefore, the data produced at regions where the underlying physical models all fail are actually empirical extrapolations. Besides, the MODIS LAI product does not provide LAI values for desert, snow, and ice land-cover surfaces, which may introduce errors when the land cover information is incorrect.

As the pre-V5 GLASS LAI algorithm is trained on the BELMANIP sites, with a latitude of up to 70°N, GLASS V5 LAI fails to provide any valid values for the vegetated land surface above 70°N throughout the year (Fig. 9e and f). The GLASS V6 training samples are globally distributed and deep learning is effective in combining the advantages of various products. The Bi-LSTM model learns the relationship between surface reflectance and LAI during the training stage. As long as there is atmospherically corrected surface reflectance above 70°N with the solar zenith angle smaller than 85°, the Bi-LSTM model can predict the valid LAI values. As for pixels with solar zenith angle larger than 85°, they are interpolated with the nearby days' valid LAI values. Therefore, compared to the above three products, the GLASS V6 LAI is spatially complete throughout the year although the uncertainties of these LAI values in very high latitudes need to be further quantified.

Fig. 10 shows the distribution of the mean LAI along the latitude for MODIS, PROB-V, GLASS V5, and V6 products in January and July 2018, respectively. Generally, the MODIS PROB-V, GLASS V5, and V6 LAI products are consistent with each other, but PROBA-V LAI is slightly higher than the others. However, for the 0°–15°S region in January, MODIS LAI shows the lowest values among these four products, while the GLASS V5 and V6 LAI profile are between PROBA-V and MODIS, and closer to PROBA-V. This can be explained by the fact that in the tropical forest area, clouds contaminate the surface reflectance for most of the year, and MODIS LAI relies on a single-time retrieval algorithm that is easily affected by cloud contamination in its input reflectance. The PROBA-V and GLASS V5 LAI apply a smooth procedure after and before retrieval, so they are not easily affected by the clouds. This result demonstrates that our deep learning model can reduce the cloud impacts automatically based on the temporal signatures of MODIS data and output the time-series continuous LAI.

Fig. 11 further displays the probability density function (PDF) of the four LAI products for different biome types in July 2018, according to MODIS land-cover product. The PDF shapes are generally consistent for shrubland (CSH and OSH), grassland, and barren sparse vegetation, while large discrepancies are observed by the forest (ENF, EBF, DNF, DBF, and MF), savanna (WSA, SAV), and crop types. Note that the savanna type usually has complicated structures, and the forest and crop types usually have large absolute LAI values. LAI estimation improvements are warranted under such conditions. For the ENF forest, GLASS V6 exhibits a narrower distribution, with a peak around 3.2, while it is about 3.5, 3.4, and 3.2 for MODIS, GLASS V5, and PROBA-V, respectively. The PROBA-V product has a higher peak LAI values for EBF, DNF, DBF, and MF than the other three. Generally, the peak value of our product is between that of the other three products.

4.5. Temporal consistency analysis

Fig. 12 presents the 21 years of the time-series LAI from MODIS, PROBA-V GLASS V5, and V6 LAI at eight DIRECT sites with different biome types from 2000 to 2020, and the corresponding time-series MODIS NDVI is shown as a reference. MODIS LAI shows more fluctuation for the forest type (Fig. 12a–d) than for other biome types (Fig. 12e–h) because the forest area experiences more cloudy and snowy conditions. PROBA-V LAI is relatively smoother than MODIS; however, a sudden drop of LAI by 2 units is observed at the ENF site in 2019 without quality flags changing, and other LAI products remain stable compared to previous years (Fig. 12b). GLASS V5 and V6 LAI exhibit smooth time-series profiles in each biome type, although the V5 LAI shows discrepancies from other products at the open shrub type (Fig. 12e). The LAI and NDVI trends are inconsistent at the Gnangara site (Fig. 12f). NDVI is about 0.1 higher in the middle of the years than in other seasons, while MODIS LAI has an opposite trend, PROBA-V has a similar trend, and GLASS V6 LAI remains stable within the years. The NDVI trend can be explained by the fact that this site is located in the woodlands in southwestern Australia, is characterized by a low cover of forest and shrub and dry background, and ~ 80% of the rain occurs from May to September, when some understory herbs appear (Veneklaas and Poot, 2003). According to previous studies, LAI in this region varies little throughout the year (about 5%) owing to the long leaf span of the prominent species, as well as the foliage renewal during different times of the year (Farrington et al., 1989; Veneklaas and Poot, 2003).

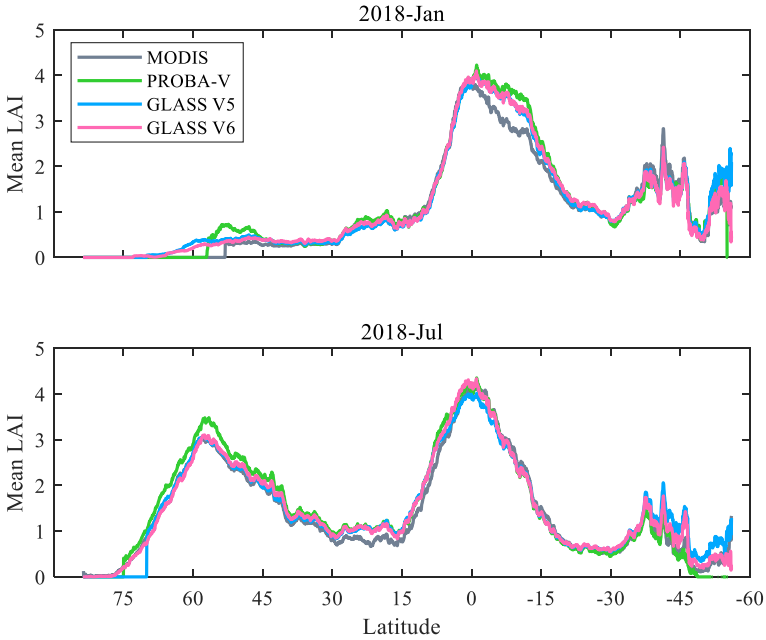

Fig. 10. Distribution of mean LAI along latitude for MODIS, PROB-V, GLASS V5, and V6 product in (a) January 2018 and (b) July 2018.

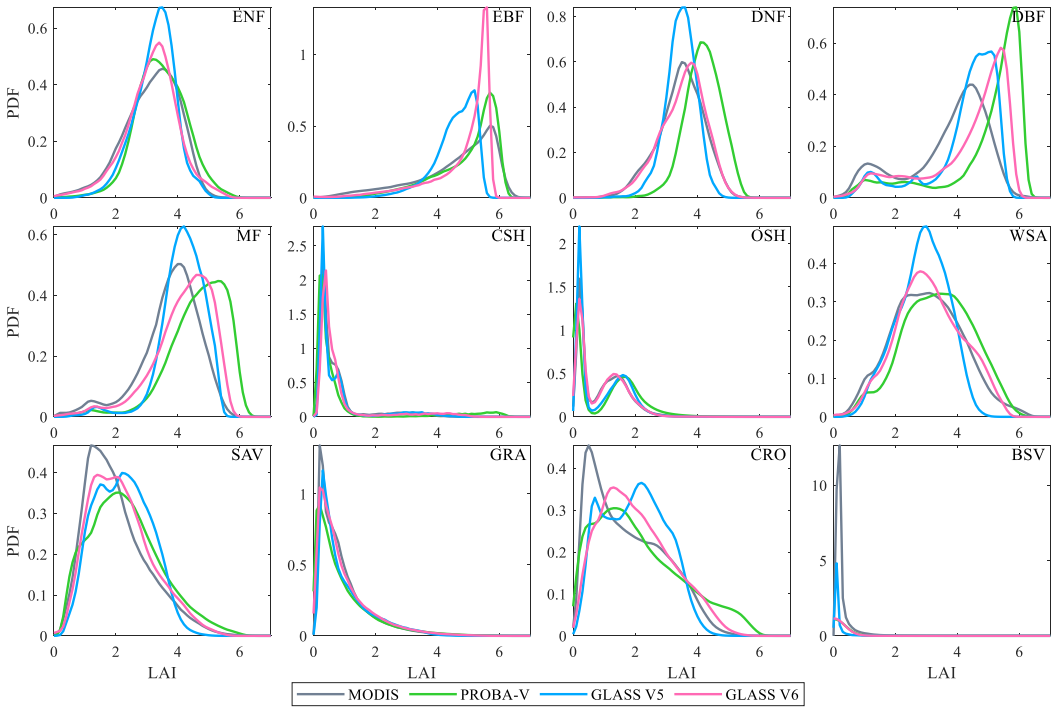

Fig. 11. Probability Density Function (PDF) with LAI bin width of 0.1 of the MODIS, PROB-V, GLASS V5, and V6 LAI for different land-cover types in July 2018.

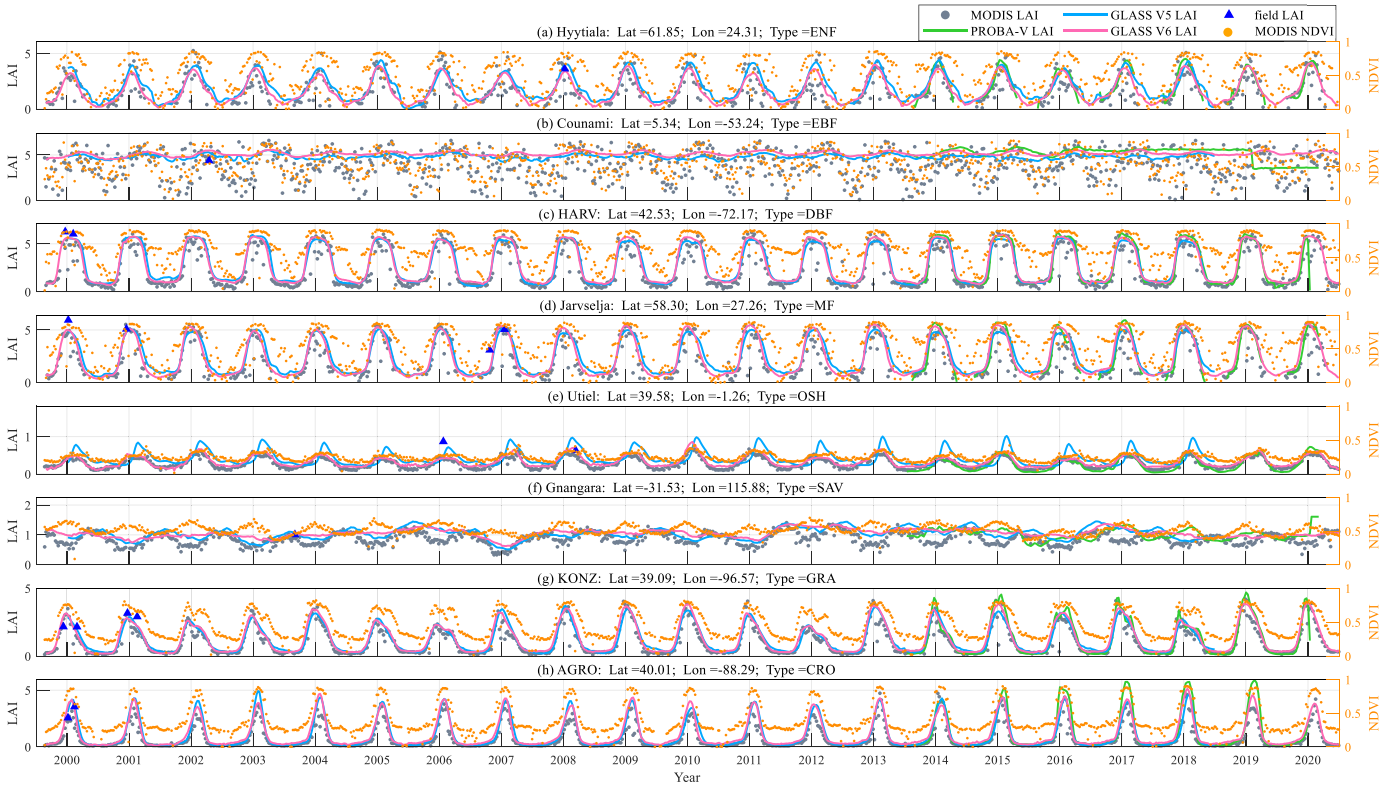

Fig. 12. Aggregated 3-km time-series LAI from MODIS, GLASS V5, GLASS V6, and PROBA-V products for eight DIRECT sites with different biome types during 2000–2020, the corresponding NDVI is added as a reference.

Therefore, the GLASS V6 LAI provides a more reasonable LAI trend than other products at this site.

These time-series plots further illustrate the quality of GLASS V6 LAI: it is time-series continuous without noise, can reflect the vegetation growth seasonality, and also corresponds well with the field measurements.

4.6. LAI trend analysis

To further evaluate the differences between GLASS V5 and V6 LAI products in characterizing the vegetation greening or browning trends, we run a linear regression analysis of temporal LAI curves on a pixel basis. The slopes of the linear regression at 0.05°are shown in Fig. 13. Overall, two versions of the GLASS LAI products show similar spatial patterns. There are some outstanding patterns, for example, the greening trends over China and the browning trends over Amazon.

The trends of the yearly average LAI values calculated from these four LAI products discussed in this paper are shown in Fig. 14. PROBA-V product has a short temporal coverage (6 years), but its annual LAI average values are close to GLASS V5 and V6 products. Note that PROBA-V LAI has decreased significantly from 2018 to 2019, while MODIS and GLASS V6 LAI are slightly increasing. MODIS LAI product shows the lowest values, which is caused by the lower values retrieved under cloudy-sky conditions, even after applying its quality control in the averaging calculation. However, the three long-term products (MODIS, GLASS V5, and GLASS V6) show similar greening trends, while the GLASS V6 product has a slightly larger increasing rate than the other two products.

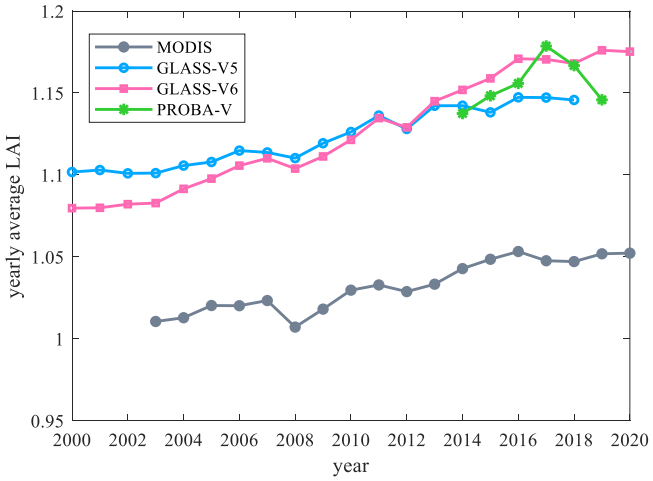

Fig. 14. Variations of the yearly average LAI values from 2000 to 2020 of the MODIS, PROBA-V, GLASS V5, and V6 products for the land surface between 70° N and − 60°S.

4.7. Improvements over the GLASS V5 LAI product

In addition to the improved accuracy and spatial continuity of GLASS V6 over V5 LAI (Section 4.3 and 4.4), the improvement of GLASS V6 also includes the temporal consistency, particularly the removal of the unrealistic seasonal variations of LAI in high latitudes of the Northern Hemisphere. We choose several pixel samples with the percentages of yearly clear-sky days (HQ) larger than 90% and randomly distributed

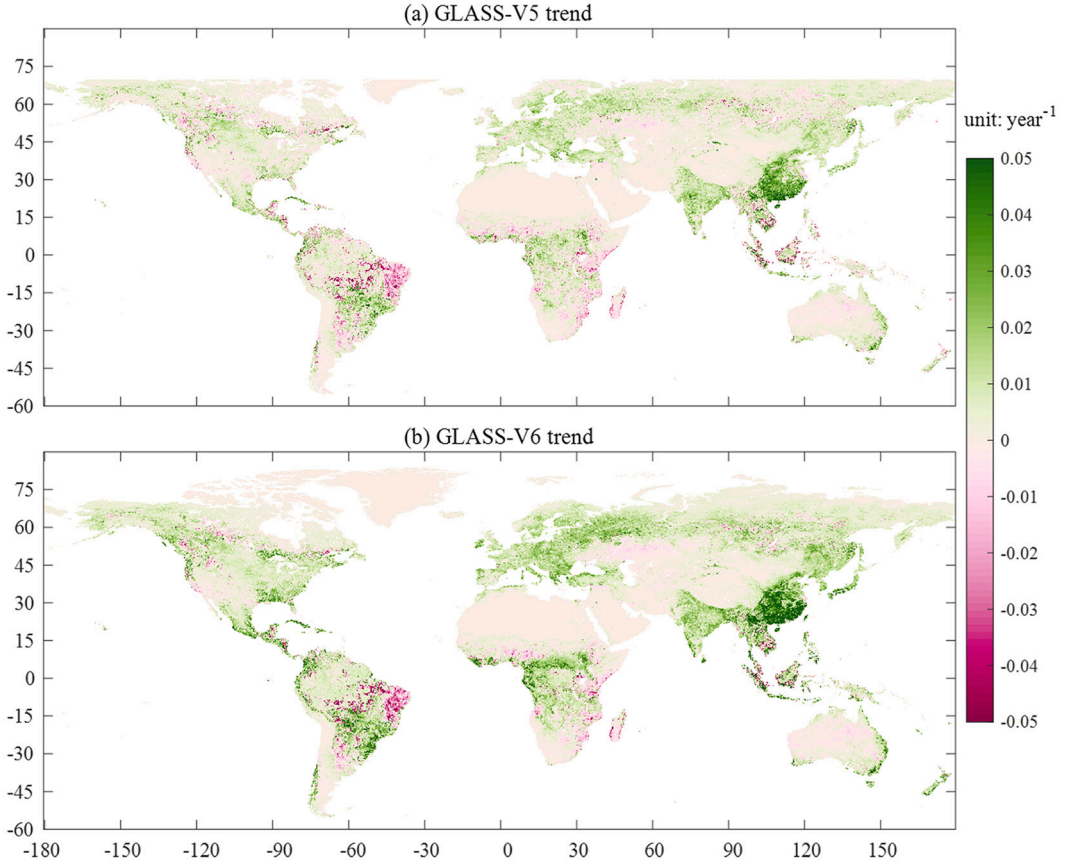

Fig. 13. Slope of the regression line fitting the temporal curve of the annual average LAI (a) GLASS V5 and (b) V6 products from 2000 to 2018; the spatial resolution is 0.05° in geographic latitude/longitude.

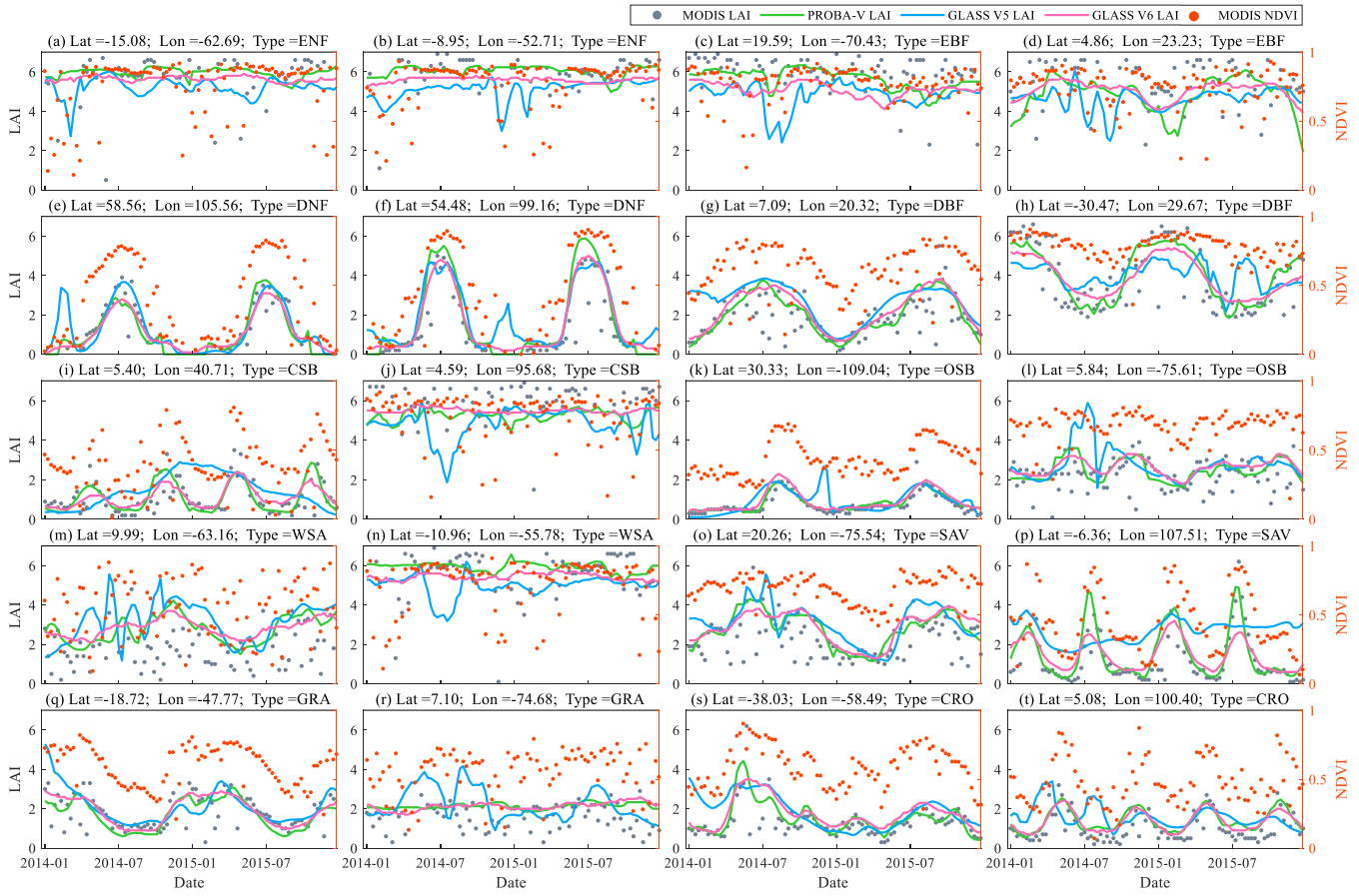

Fig. 15. Time-series LAI from MODIS, GLASS V5, GLASS V6, and PROBA-V products for sample pixels with different biome types from 2014 to 2015, the corresponding NDVI is added as reference (only the high-quality MODIS LAI (QC $\geq$ 64) is shown).

from −40°S to 60°N to show the differences from GLASS V5 LAI, and add the corresponding MODIS NDVI as a reference. As shown in Fig. 15, the first issue in GLASS V5 LAI is the instability compared to GLASS V6 for ENF and EBF pixels (Fig. 15a–d), and the second is the unrealistic growing cycle for DNF, DBF, and shrubland pixels (Fig. 15e, f, g, and k). Moreover, it fails to detect the multi-growing cycles for savanna and croplands in Fig. 15p and 15 t. Compared to GLASS V5, GLASS V6 LAI is more temporally consistent and better reflects the growing seasonality of different vegetation types.

The previous GLASS LAI algorithm relies on the noise-removed reconstructed surface reflectance to derive a temporal continuous product. The reconstruction method is based on the temporal continuous vegetation index, which may cause significant errors when there are no clear-sky observations over long periods, such as in cloud- or snow-dominated winters in the high latitude of the northern hemisphere, monsoon-dominated regions during the rainy seasons, or cloud-dominated tropical areas. Here, we also show some cases under special conditions where HQ ranges from 24%–63% in Fig. 16. For the EBF forests distributed in the cloud-dominated tropical areas (Fig. 16a-d), the HQ is lowest within the range from 24%–32%, when both GLASS V5 and PROBA-V LAI show fluctuations, while GLASS V6 exhibits a more stable time series trend. For the ENF forest distributed above 55°N with an HQ of ~60% (Fig. 16e-h), GLASS V6 shows similar seasonal trends to MODIS and PROBA-V LAI, while GLASS V5 has oscillations and fake growing seasons. For the DNF forest distributed above 65°N with HQ of ~50% (Fig. 16i-l), these four products exhibit the similar growing seasonality, the only difference is whether the very low LAI values during winter time have been provided or not. For vegetation types above 70°N with HQ of ~40% (Fig. 16 m-p), GLASS V5 does not provide any values during the whole year, while GLASS V6 still captures the vegetation variation and corresponds well with MODIS and PROBA-V LAI when they contain high-quality values.

5. Discussion

As different biomes have different canopy structures, in theory, the land-cover map can be added as a category variable and improve the model performance, but in reality, land-cover maps are not always accurate, as the classification errors for certain land-cover types can be large. During the Bi-LSTM model training process, the data samples with different biome types are combined to reduce the uncertainties introduced by land-cover products in the LAI production step. To compare with the biome-independent model, we also construct the Bi-LSTM models for six biome-types (similar to MODIS LAI algorithm) under the best band combination and temporal length (see Section 4.2) conditions. Statistics (Table S3) show that these two kinds of models achieve similar accuracies; besides, there is no significant bias for different biome types, indicating that the biome-independent Bi-LSTM model for global LAI estimation is robust enough to account for the information of each IGBP biome-type. Thus, there is no need to include the land-cover map in the LAI production.

Although several global LAI products have been generated from different satellite observations, they still fall short of the requirements of many applications. For example, the GCOS requires the global LAI products to have a spatial resolution of 250 m, daily temporal frequency, and accuracy of 15% for better simulations of climate and carbon-cycle models (GCOS, 2016). The GLASS-V6 LAI product presented in this paper is the first global long-term LAI product at the 250-m resolution. It

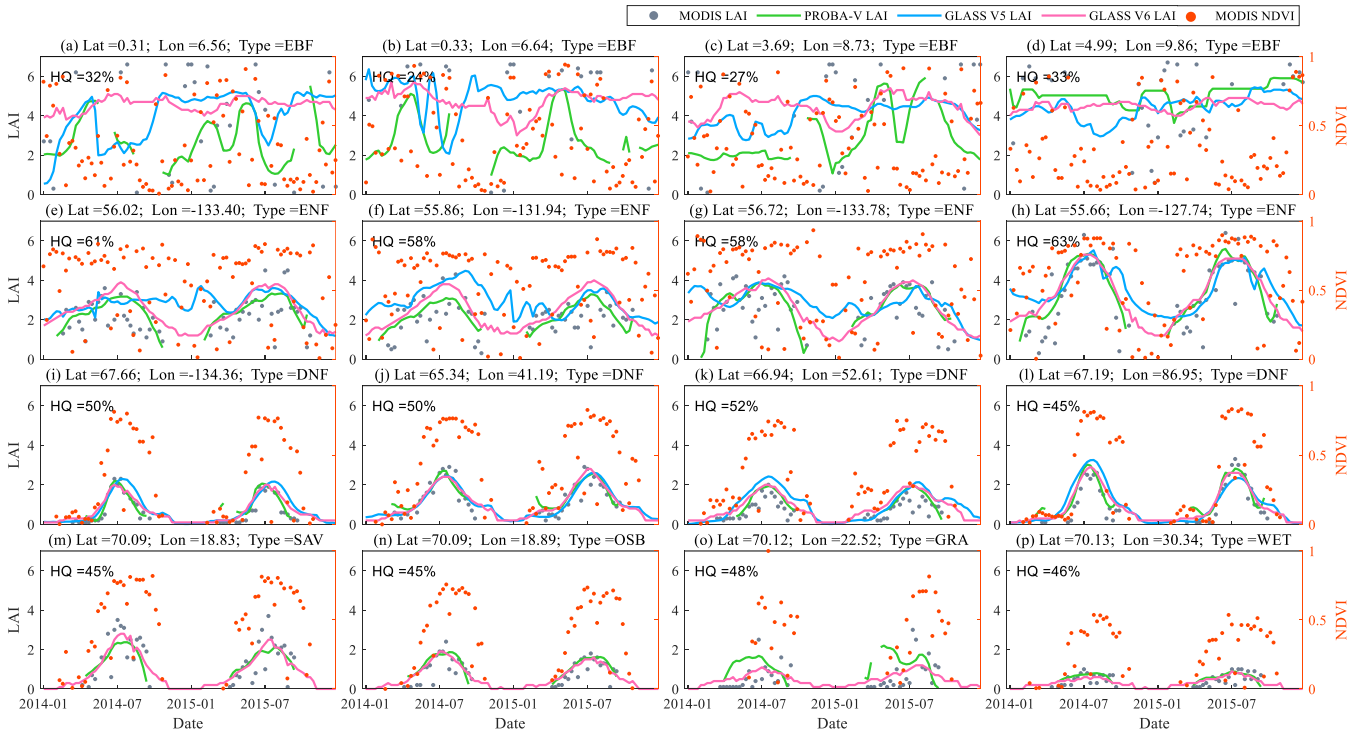

Fig. 16. Time-series LAI from MODIS, GLASS V5, GLASS V6, and PROBA-V products for sample pixels under special conditions from 2014 to 2015, the corresponding NDVI is added as reference (only the high-quality MODIS LAI (QC $\geq$ 64) is shown, the percentage of MODIS high-quality retrievals (HQ) ranges from 24% to 63%).

can meet the spatial resolution requirement but fails to meet the GCOS requirements of temporal resolution and accuracy, although the GLASS V6 LAI product is more accurate than other products compared in this study based on the direct validation. There may be several solutions to explore for more accurate LAI retrievals at pixel scale. For the physical-model based LAI retrieval methods, the first direction is to develop more accurate forward models that account for the canopy structure, soil, and leaf bi-directional reflectance properties. Another solution is to use more satellite observations by integrating satellite data at different spatial and temporal resolutions (e.g., different geostationary satellite data or polar-orbiting satellite data at different spatial resolutions), and to incorporate different sources of prior information to regulate the inversion (Ma et al., 2020; Ma et al., 2022). With improved LAI retrievals at the pixel/site scale, the statistical methods can benefit from the higher-quality training dataset. Third, more machine learning methods should be further compared and evaluated in the LAI estimation, such as Gaussian Process Regression (Svendsen et al., 2020; Verrelst et al., 2013) and Random Forest (Houborg and McCabe, 2018; Kang et al., 2021), and new deep learning methods can be further combined and explored to take better advantage of the signatures of satellite data, such as convolutional neural networks, which can use the contextual signatures of remote sensing images (Chai et al., 2019; Li et al., 2021).

The GLASS V6 LAI has a temporal resolution of 8 days, but there is no global daily LAI product that has been officially released yet. Technically the trained model can output the daily LAI by taking MODIS daily surface reflectance product (MOD09GA) as an input; however, whether the model can capture the daily variations of the land surface still needs further evaluation. The other feasible approach is to create the global training LAI samples at the daily resolution. This can be achieved by retrieving LAI at the representative pixels from the abovementioned directions. Besides, the 250-m LAI estimation model is developed from the 500-m data product in this study considering that these two resolutions are close. However, this may introduce uncertainties to some degree due to the pixel heterogeneity (Tian et al., 2003). If the difference in spatial resolution is too large, this assumption may not be appropriate. Note that the 500-m GLASS V6 LAI has been aggregated to 0.05° and 0.5° spatial resolutions for wider users.

The Bi-LSTM can produce smoother and more continuous predictions even with noisy inputs, but the changing rate of the smoothed time series may not always correspond to extreme values that highlight important ecological changes/disturbances (Fig. S2). Further study is needed using in situ measurements to evaluate whether additional information on land cover, particularly on rapid or abrupt land-cover changes is beneficial for the algorithm performance.

At last, in situ measurement networks under different conditions, especially under cloud-dominated tropical or high latitude areas, need to be expanded at the international level, for a more comprehensive and objective assessment of current global LAI products, and understanding of the LAI seasonal and yearly variations.

6. Conclusion

A deep learning Bi-LSTM model is applied to generate a 21-year (from 2000 to 2020) global spatiotemporally continuous LAI product at a spatial resolution of 250 m, which is denoted as the GLASS LAI V6 product. The new model takes advantage of the existing global LAI products and the temporal information of MODIS surface reflectance effectively.

A global sampling strategy is first applied to generate the fused time-series LAI samples from three existing global LAI products (MODIS C6, GLASS V5, and PROBA-V V1) when their values are the closest over major land surface types. A total of 52,997 samples are selected and then divided into training (70%), validation (20%), and test (10%) datasets. Four machine learning models are explored, and the Bi-LSTM outperforms the GRNN, LSTM, and GRU in learning the temporal relationship between MODIS surface reflectance and LAI, and is used in generating the GLASS V6 LAI product. The Bi-LSTM model is established using six bands (except band 5) and the first two bands of 500-m MODIS surface reflectance, respectively. The RMSE values based on the test dataset are 0.266 (six-band model) and 0.283(two-band model). The

two-band Bi-LSTM model is then applied to 250-m surface reflectance, and the estimated LAI values are normalized by those estimated using the six-band model at 500-m spatial resolution.

Evaluation of the GLASS LAI V6 product is based on both validation using in-situ measurements and comparisons with the existing LAI products. Validation using 79 LAI high-resolution reference maps shows that the GLASS V6 LAI product at both 250-m and 500-m resolutions is more accurate with the RMSE of 0.92 and 0.86, compared to PROBA-V V1 LAI at 300 m and MODIS C6 and GLASS V5 LAI at 500 m (RMSE of 0.98, 1.08, and 0.95, respectively). Comparisons with existing products show that GLASS V6 LAI has better spatial and temporal consistency (Sections 4.4 and 4.5). The improvements over GLASS V5 LAI product include better spatial continuity throughout the year and higher temporal consistency in capturing the vegetation growing cycles. The GLASS V6 LAI product also shows a similar vegetation greening trend to that of GLASS V5 and MODIS.

The Bi-LSTM LAI estimation model used in this study has several characteristics. First, the computational efficiency is greatly improved because the pre-processing of surface reflectance for smoothing and gap-filling is avoided. Second, the quality of the estimated new LAI values is not significantly degraded when the high-quality surface reflectance is absent for a long period owing to persistent cloud or snow cover. The main reason is likely that the Bi-LSTM model can extract information across 2-year surface reflectance rather than a single time point.

Credit author statement

Han Ma performed data curation, investigation, methodology, validation, and writing- original draft preparation; Shunlin Liang performed conceptualization, resources, supervision, writing- review and editing.

Declaration of Competing Interest

The authors declare that they have no known competing financial interests or personal relationships that could have appeared to influence the work reported in this paper.

Acknowledgments

This study was partially supported by the National Key Research and Development Program of China (No. 2016YFA0600103) and China Postdoctoral Science Foundation Grant (2019M652707). We would like to thank NASA, CGLS, and BNU for providing MODIS, PROBA-V, and GLASS data products, and the principal investigators of Bigfoot, VALERI, and ImagineS networks for providing LAI reference data. We gratefully acknowledge the data support from "National Earth System Science Data Center, National Science &Technology Infrastructure of China (http://www.geodata.cn)". We thank Jianming Yin, Qian Wang, and Longping Si for their help during the data production. We are also grateful to the four anonymous reviewers for their constructive comments and suggestions. The updated algorithm with the reviewers' inputs has been used for generating the GLASS Version 6 LAI product.

Appendix A. Supplementary data

Supplementary data to this article can be found online at https://doi.org/10.1016/j.rse.2022.112985.

References

Alkama, R., Forzieri, G., Duveiller, G., Grassi, G., Liang, S., Cescatti, A., 2022. Vegetation-based climate mitigation in a warmer and greener world. Nat. Commun. 13, 1–10.

Ball, J.E., Anderson, D.T., Chan, C.S., 2017. Comprehensive survey of deep learning in remote sensing: theories, tools, and challenges for the community. J. Appl. Remote. Sens. 11, 042609.

Baret, F., Morissette, J.T., Fernandes, R., Champeaux, J.L., Myneni, R.B., Chen, J., Plummer, S., Weiss, M., Bacour, C., Garrigues, S., 2006. Evaluation of the representativeness of networks of sites for the global validation and intercomparison of land biophysical products: proposition of the CEOS-BELMANIP. IEEE Trans. Geosci. Remote Sens. 44, 1794–1803.

Baret, F., Hagolle, O., Geiger, B., Bicheron, P., Miras, B., Huc, M., Berthelot, B., Niño, F., Weiss, M., Samain, O., 2007. LAI, fAPAR and fCover CYCLOPES global products derived from VEGETATION: part 1: principles of the algorithm. Remote Sens. Environ. 110, 275–286.

Baret, F., Weiss, M., Allard, D., Garrigues, S., Leroy, M., Jeanjean, H., Fernandes, R., Myneni, R., Privette, J., Morisette, J., 2021. VALERI: a network of sites and a methodology for the validation of medium spatial resolution land satellite products. ⟨hal-03221068⟩.

Baret, F., Weiss, M., Lacaze, R., Camacho, F., Makhmara, H., Pacholcyzk, P., Smets, B., 2013. GEOV1: LAI and FAPAR essential climate variables and FCOVER global time series capitalizing over existing products. Part1: principles of development and production. Remote Sens. Environ. 137, 299–309.

Baret, F., Weiss, M., Verger, A., Smets, B., 2016a. Atbd for Lai, Fapar and Fcover from Proba-V Products at 300 Mresolution (Geov3). Imagines_rp2. 1_atbd-lai, p. 300.

Baret, F., Weiss, M., Verger, A., Smets, B., 2016b. Atbd For Lai, Fapar And Fcover From Proba-V Products At 300m Resolution (Geov3). Imagines_rp2. 1_atbd-lai, p. 300.

Brown, L.A., Meier, C., Morris, H., Pastor-Guzman, J., Bai, G., Lerebourg, C., Gobron, N., Lanconelli, C., Clerici, M., Dash, J., 2020. Evaluation of global leaf area index and fraction of absorbed photosynthetically active radiation products over North America using Copernicus ground based observations for validation data. Remote Sens. Environ. 247, 111935.

Caliński, T., Harabasz, J., 1974. A dendrite method for cluster analysis. Commun. Stat. Theor. Method 3, 1–27.

Chai, D., Newsam, S., Zhang, H.K., Qiu, Y., Huang, J., 2019. Cloud and cloud shadow detection in Landsat imagery based on deep convolutional neural networks. Remote Sens. Environ. 225, 307–316.

Chen, J.M., Black, T., 1992. Defining leaf area index for non-flat leaves. Plant Cell Environ. 15, 421–429.

Chen, J., Menges, C., Leblanc, S., 2005. Global mapping of foliage clumping index using multi-angular satellite data. Remote Sens. Environ. 97, 447–457.

Cho, K., Van Merriënboer, B., Gulcehre, C., Bahdanau, D., Bougares, F., Schwenk, H., Bengio, Y., 2014. Learning Phrase Representations using RNN Encoder-Decoder for Statistical Machine Translation arXiv preprint arXiv:1406.1078.

Fang, H., Liang, S., 2003. Retrieving leaf area index with a neural network method: simulation and validation. IEEE Trans. Geosci. Remote Sens. 41, 2052–2062.

Fang, H., Baret, F., Plummer, S., Schaepman-Strub, G., 2019a. An overview of global leaf area index (LAI): methods, products, validation, and applications. Rev. Geophys. 57, 739–799.

Fang, K., Pan, M., Shen, C., 2019b. The value of SMAP for long-term soil moisture estimation with the help of deep learning. IEEE Trans. Geosci. Remote Sens. 57, 2221–2233.

Farrington, P., Greenwood, E., Bartle, G., Beresford, J., Watson, G., 1989. Evaporation from Banksia woodland on a groundwater mound. J. Hydrol. 105, 173–186.

Feng, D., Chen, J.M., Plummer, S., Mingzhen, C., Pisek, J., 2006. Algorithm for global leaf area index retrieval using satellite imagery. IEEE Trans. Geosci. Remote Sens. 44, 2219–2229.

Fuster, B., Sánchez-Zapero, J., Camacho, F., García-Santos, V., Verger, A., Lacaze, R., Weiss, M., Baret, F., Smets, B., 2020. Quality assessment of PROBA-V LAI, fAPAR and fCOVER collection 300 m products of Copernicus global land service. Remote Sens. 12.

Garrigues, S., Lacaze, R., Baret, F., Morisette, J., Weiss, M., Nickeson, J., Fernandes, R., Plummer, S., Shabanov, N., Myneni, R., 2008. Validation and intercomparison of global leaf area index products derived from remote sensing data. J. Geophys. Res. Biogeosci. 113.

GCOS, 2016. The Global Observing System for Climate: Implementation Needs, GCOS-200, GOOS-214.

Gonsamo, A., Chen, J.M., 2014. Improved LAI algorithm implementation to MODIS data by incorporating background, topography, and foliage clumping information. IEEE Trans. Geosci. Remote Sens. 52, 1076–1088.

Gower, S.T., Kirschbaum, A.A., 2008. BigFoot Field Data for North American Sites, 1999–2003. ORNL Distributed Active Archive Center.

Graves, A., Schmidhuber, J., 2005. Framewise phoneme classification with bidirectional LSTM and other neural network architectures. Neural Netw. 18, 602–610.

He, L., Chen, J.M., Pisek, J., Schaaf, C.B., Strahler, A.H., 2012. Global clumping index map derived from the MODIS BRDF product. Remote Sens. Environ. 119, 118–130.

Hochreiter, S., Schmidhuber, J., 1997. Long short-term memory. Neural Comput. 9, 1735–1780.

Holben, B.N., 1986. Characteristics of maximum-value composite images from temporal AVHRR data. Int. J. Remote Sens. 7, 1417–1434.

Houborg, R., McCabe, M.F., 2018. A hybrid training approach for leaf area index estimation via cubist and random forests machine-learning. ISPRS J. Photogramm. Remote Sens. 135, 173–188.

Huang, Z., Xu, W., Yu, K., 2015. Bidirectional LSTM-CRF Models for Sequence Tagging arXiv preprint arXiv:1508.01991.

Jacquemoud, S., Verhoef, W., Baret, F., Bacour, C., Zarco-Tejada, P.J., Asner, G.P., François, C., Ustin, S.L., 2009. PROSPECT+SAIL models: a review of use for vegetation characterization. Remote Sens. Environ. 113, S56–S66.

Jiang, C., Ryu, Y., Fang, H., Myneni, R., Claverie, M., Zhu, Z., 2017. Inconsistencies of interannual variability and trends in long-term satellite leaf area index products. Glob. Chang. Biol. 23, 4133–4146.

Jiang, H., Hu, H., Zhong, R., Xu, J., Xu, J., Huang, J., Wang, S., Ying, Y., Lin, T., 2020. A deep learning approach to conflating heterogeneous geospatial data for corn yield estimation: a case study of the US Corn Belt at the county level. Glob. Chang. Biol. 26, 1754–1766.
Jin, H., Li, A., Bian, J., Nan, X., Zhao, W., Zhang, Z., Yin, G., 2017. Intercomparison and validation of MODIS and GLASS leaf area index (LAI) products over mountain areas: a case study in southwestern China. Int. J. Appl. Earth Obs. Geoinf. 55, 52–67.
Justice, C., Belward, A., Morisette, J., Lewis, P., Privette, J., Baret, F., 2000. Developments in the'validation'of satellite sensor products for the study of the land surface. Int. J. Remote Sens. 21, 3383–3390.
Kang, Y., Özdoğan, M., Zipper, C.S., Román, O.M., Walker, J., Hong, Y.S., Marshall, M., Magliulo, V., Moreno, J., Alonso, L., Miyata, A., Kimball, B., Loheide, P.S., 2016. How universal is the relationship between remotely sensed vegetation indices and crop leaf area index? a global assessment. Remote Sens. 8, 597.
Kang, Y., Ozdogan, M., Gao, F., Anderson, M.C., White, W.A., Yang, Y., Yang, Y., Erickson, T.A., 2021. A data-driven approach to estimate leaf area index for Landsat images over the contiguous US. Remote Sens. Environ. 258, 112383.
Li, X., Lu, H., Yu, L., Yang, K., 2018. Comparison of the spatial characteristics of four remotely sensed leaf area index products over China: direct validation and relative uncertainties. Remote Sens. 10, 148.
Li, Y., Liu, H., Ma, J., Zhang, L., 2021. Estimation of leaf area index for winter wheat at early stages based on convolutional neural networks. Comput. Electron. Agric. 190, 106480.
Liang, S., Wang, J., 2019. Advanced Remote Sensing: Terrestrial Information Extraction and Applications. Academic Press.
Liang, S., Cheng, J., Jia, K., Jiang, B., Liu, Q., Xiao, Z., Yao, Y., Yuan, W., Zhang, X., Zhao, X., 2021. The global land surface satellite (GLASS) product suite. Bull. Am. Meteorol. Soc. 102, E323–E337.
Liu, Y., Liu, R., Chen, J.M., 2012. Retrospective retrieval of long-term consistent global leaf area index (1981–2011) from combined AVHRR and MODIS data. J. Geophys. Res. Biogeosci. 117.
Ma, H., Liang, S., Shi, H., Zhang, Y., 2020. An optimization approach for estimating multiple land surface and atmospheric variables from the geostationary advanced Himawari imager top-of-atmosphere observations. IEEE Trans. Geosci. Remote Sens. 1–21.
Ma, H., Liang, S., Zhu, Z., He, T., 2022. Developing a land continuous variable estimator to generate daily land products from Landsat data. IEEE Trans. Geosci. Remote Sens. 60, 1–19.
Myneni, R.B., Hoffman, S., Knyazikhin, Y., Privette, J., Glassy, J., Tian, Y., Wang, Y., Song, X., Zhang, Y., Smith, G., 2002. Global products of vegetation leaf area and fraction absorbed PAR from year one of MODIS data. Remote Sens. Environ. 83, 214–231.
Myneni, R., Knyazikhin, Y., Park, T., 2015. MOD15A2H MODIS/Terra Leaf Area Index/FPAR 8-Day L4 Global 500m SIN Grid V006. NASA EOSDIS Land Processes DAAC. https://doi.org/10.5067/MODIS/MOD15A2H.006.
Piao, S., Yin, G., Tan, J., Cheng, L., Huang, M., Li, Y., Liu, R., Mao, J., Myneni, R.B., Peng, S., 2015. Detection and attribution of vegetation greening trend in China over the last 30 years. Glob. Chang. Biol. 21, 1601–1609.
Saltelli, A., Annoni, P., Azzini, I., Campolongo, F., Ratto, M., Tarantola, S., 2010. Variance based sensitivity analysis of model output. Design and estimator for the total sensitivity index. Comput. Phys. Commun. 181, 259–270.
Shen, H.F., Jiang, Y., Li, T.W., Cheng, Q., Zeng, C., Zhang, L.P., 2020. Deep learning-based air temperature mapping by fusing remote sensing, station, simulation and socioeconomic data. Remote Sens. Environ. 240.
Sherstinsky, A., 2020. Fundamentals of recurrent neural network (RNN) and long short-term memory (LSTM) network. Physica D: Nonlinear Phenomena 404, 132306.
Specht, D.F., 1991. A general regression neural network. IEEE Trans. Neural Netw. 2, 568–576.
Sulla-Menashe, D., Friedl, M.A., 2018. User Guide to Collection 6 MODIS Land Cover (MCD12Q1 and MCD12C1) Product. USGS, Reston, VA, USA, pp. 1–18.
Svendsen, D.H., Morales-Álvarez, P., Ruescas, A.B., Molina, R., Camps-Valls, G., 2020. Deep Gaussian processes for biogeophysical parameter retrieval and model inversion. ISPRS J. Photogramm. Remote Sens. 166, 68–81.
Thireou, T., Reczko, M., 2007. Bidirectional long short-term memory networks for predicting the subcellular localization of eukaryotic proteins. IEEE/ACM Trans. Comput. Biol. Bioinform. 4.
Tian, Y., Wang, Y., Zhang, Y., Knyazikhin, Y., Bogaert, J., Myneni, R.B., 2003. Radiative transfer based scaling of LAI retrievals from reflectance data of different resolutions. Remote Sens. Environ. 84, 143–159.
Veneklaas, E.J., Poot, P., 2003. Seasonal patterns in water use and leaf turnover of different plant functional types in a species-rich woodland, South-Western Australia. Plant Soil 257, 295–304.
Vermote, E.F., Ray, J.P., 2015. MODIS Surface Reflectance User's Guide Collection, 6, pp. 1–37.
Verrelst, J., Rivera, J.P., Moreno, J., Camps-Valls, G., 2013. Gaussian processes uncertainty estimates in experimental Sentinel-2 LAI and leaf chlorophyll content retrieval. ISPRS J. Photogramm. Remote Sens. 86, 157–167.
Wu, X., Xiao, Q., Wen, J., You, D., Hueni, A., 2019. Advances in quantitative remote sensing product validation: overview and current status. Earth Sci. Rev. 196, 102875.
Wu, H.C., Yang, Q.L., Liu, J.M., Wang, G.Q., 2020. A spatiotemporal deep fusion model for merging satellite and gauge precipitation in China. J. Hydrol. 584, 124664.
Xiao, Z., Liang, S., Wang, J., Chen, P., Yin, X., Zhang, L., Song, J., 2014. Use of general regression neural networks for generating the GLASS leaf area index product from time-series MODIS surface reflectance. IEEE Trans. Geosci. Remote Sens. 52, 209–223.
Xiao, Z., Liang, S., Wang, T., Liu, Q., 2015. Reconstruction of satellite-retrieved land-surface reflectance based on temporally-continuous vegetation indices. Remote Sens. 7, 9844–9864.
Xu, B., Li, J., Park, T., Liu, Q., Zeng, Y., Yin, G., Zhao, J., Fan, W., Yang, L., Knyazikhin, Y., Myneni, R.B., 2018. An integrated method for validating long-term leaf area index products using global networks of site-based measurements. Remote Sens. Environ. 209, 134–151.
Yan, K., Park, T., Yan, G., Chen, C., Yang, B., Liu, Z., Nemani, R.R., Knyazikhin, Y., Myneni, R.B., 2016a. Evaluation of MODIS LAI/FPAR product collection 6. Part 1: consistency and improvements. Remote Sens. 8, 359.
Yan, K., Park, T., Yan, G., Liu, Z., Yang, B., Chen, C., Nemani, R., Knyazikhin, Y., Myneni, R., 2016b. Evaluation of MODIS LAI/FPAR product collection 6. Part 2: validation and Intercomparison. Remote Sens. 8, 460.
Yan, G., Hu, R., Luo, J., Weiss, M., Jiang, H., Mu, X., Xie, D., Zhang, W., 2019. Review of indirect optical measurements of leaf area index: recent advances, challenges, and perspectives. Agric. For. Meteorol. 265, 390–411.
Yildirim, Ö., 2018. A novel wavelet sequence based on deep bidirectional LSTM network model for ECG signal classification. Comput. Biol. Med. 96, 189–202.
Yuan, Q., Shen, H., Li, T., Li, Z., Li, S., Jiang, Y., Xu, H., Tan, W., Yang, Q., Wang, J., Gao, J., Zhang, L., 2020. Deep learning in environmental remote sensing: achievements and challenges. Remote Sens. Environ. 241, 111716.